A three-field based optimization formulation for flow simulations in networks of fractures on non-conforming meshes

SIAM J. SCI. COMPUT.
Vol. 43, No. 2, pp. B381–B404

A THREE-FIELD BASED OPTIMIZATION FORMULATION FOR FLOW SIMULATIONS IN NETWORKS OF FRACTURES ON NONCONFORMING MESHES*

STEFANO BERRONE†, DENISE GRAPPEIN†, SANDRA PIERACCINI‡, AND STEFANO SCIALÓ†

Abstract. A new numerical scheme is proposed for flow computation in complex discrete fracture networks. The method is based on a three-field domain decomposition framework in which independent variables are introduced at the interfaces generated in the process of decoupling the original problem on the whole network into a set of fracture-local problems. A PDE-constrained formulation is then used to enforce compatibility conditions at the interfaces. The combination of the three-field domain decomposition and of the optimization-based coupling strategy results in a novel method which can handle nonconforming meshes, independently built on each geometrical object of the computational domain, and ensures a local mass conservation property at fracture intersections, which is of paramount importance for hydrogeological applications. An iterative solver is devised for the method, suitable for parallel implementation on parallel computing architectures.

Key words. discrete fracture networks, Darcy law, PDE-constrained optimization, extended finite elements, nonconforming mesh

AMS subject classifications. 65N30, 65N15, 65N50, 65J15

DOI. 10.1137/20M1319188

1. Introduction.

The present work proposes a new numerical approach for flow simulations in fracture networks, described by means of the discrete fracture network (DFN) model. The method combines a three-field–based domain decomposition strategy [14] to a PDE-constrained approach [8] for the imposition of interface conditions. The resulting approach inherits the robustness with respect to geometrical complexity and the predisposition to parallel implementation given by the optimization framework and exhibits an improved flexibility and new approximation properties resulting from the used domain decomposition method.

DFNs are sets of intersecting planar polygons arbitrarily oriented in the three-dimensional space, representing fractures in underground rock formations, and are typically generated sampling hydraulic and geological soil properties from probability distribution functions [15, 20, 19]. DFN models provide an explicit representation of fractures and thus are a viable alternative to homogenization-based approaches [5], when the presence of a network of fractures sensibly affects relevant flow characteristics. In fact, flow directionality and preferential paths might not be correctly accounted for by using homogenized properties for rocks and fractures [21, 33]. When fracture hydraulic transmissivity is much higher than rock transmissivity, the influence of the porous rock matrix can be neglected, with minor impact on the prediction of the flow.

*Submitted to the journal's Computational Methods in Science and Engineering section February 18, 2020; accepted for publication (in revised form) October 26, 2020; published electronically March 16, 2021.

https://doi.org/10.1137/20M1319188

Funding: This work was supported by the MIUR project "Dipartimenti di Eccellenza 2018-2022" (CUP E11G18000350001), by the PRIN project "Virtual Element Methods: Analysis and Applications" (201744KLJL_004), and by INdAM-GNCS.

†Dipartimento di Scienze Matematiche, Politecnico di Torino, Torino 10129, Italy (stefano.berrone@polito.it, denise.grappein@polito.it, stefano.scialo@polito.it).

‡Ingegneria Meccanica e Aerospaziale, Politecnico di Torino, Torino 10129, Italy (sandra.pieraccini@polito.it).

A major drawback for DFN flow simulations is related to the geometrical complexity and size of the resulting computational domains, which might count a large number of fractures, with dimensions ranging from centimeters to kilometers and forming an intricate network of intersections, where suitable conditions need to be enforced to couple the solution on the intersecting fractures. This complex multiscale geometrical nature of DFN domains significantly limits the applicability of conventional numerical simulation tools which rely on mesh conformity to enforce interface conditions, as it is often a very difficult task to generate good-quality conforming meshes of realistic DFNs, even introducing a large number of unknowns [17, 1, 24].

Recently, many different approaches have been suggested to overcome such a difficulty. A possible strategy consists in a dimensional reduction of the problem: In [18, 13] the DFN is replaced by a set of one-dimensional channels or pipes resembling the connections among fractures in the network; in [29] the problems on the fractures are rewritten in terms of the one-dimensional interface unknowns only, whereas in [28, 25, 34] DFNs are analyzed using graph theory tools. Some authors propose new efficient meshing strategies for complex networks, aiming at obtaining a conforming mesh with minor modifications of network geometry [22] or replacing hard-to-mesh configurations with stochastically equivalent analog, which are easier to mesh [26, 27]. Discretization methods capable of handling polygonal meshes are also suggested as effective strategies to obtain conforming meshes of complex networks: The use of virtual elements proposed in [2, 3, 23, 6], mimetic finite differences in [1], and hybrid high-order methods in [16] are some relevant examples. Other authors suggest the use of mortaring techniques to partially alleviate the conformity requirement at fracture intersections, [36, 31, 32].

A different approach is proposed in [8, 10, 11], which relies on numerical optimization to enforce interface conditions, without requiring any mesh conformity at fracture intersections and thus completely overcoming any problem related to mesh generation. The method is based on a domain decomposition framework applied to the fracture network, where one variable is introduced at each fracture intersection for each intersecting fracture, accounting for the unknown flux exchange, and then a cost functional, expressing the error in continuity and flux balance at the interfaces, is minimized constrained by a set of PDEs defined on each fracture to recover the solution on the whole network. The method is robust to complex geometries and highly efficient thanks to its predisposition to parallel implementation [7, 12].

Here, while keeping a similar optimization framework, a new formulation is proposed for the constraint equations, based on the *three-field* formulation suggested in [14]. Two unknowns are introduced at each interface, representing the unknown flux exchanged by the two intersecting fractures and the unknown trace of the hydraulic head, which, together with the primal variable, form three independent fields. The resulting approach retains the capability of dealing with nonconforming meshes and the predisposition to parallel implementation given by the optimization formulation, providing, at the same time, new approximation capabilities to the method. A key aspect is the new structure of the cost functional: While in the original optimization formulation the functional is given by the sum of two terms, one expressing the error in solution continuity at the interfaces and another for flux mismatch at the interfaces, the new proposed functional only measures the error in continuity at the interfaces, thus avoiding possible unbalance between the different terms, with a positive impact on the minimization process. Flux balance at each trace is, indeed, intrinsically enforced in the proposed three-field formulation, and this is another relevant aspect of the method, which has local mass conservation properties.

The manuscript is organized as follows. In section 2 a three-field formulation of the Darcy problem in fracture networks is written and recast into a PDE-constrained formulation suitable for discretization on nonconforming meshes. The resulting discrete approach is shown in section 3. Section 4 reports well-posedness results for the discrete problem, section 5 proposes the algorithm to compute the numerical solution, and section 6 describes some numerical examples. Concluding remarks are finally proposed in section 7.

2. Continuous model. The present section is devoted to the presentation of a three-field formulation for the Darcy problem. In the first subsection, a classical formulation is proposed, introducing the equations and the coupling conditions at the interfaces, whereas in the second subsection a novel optimization formulation is described. In the following, $\mathrm{L}^2(\omega)$ is the Hilbert space on ω of square integrable functions, and $\mathrm{H}^r(\omega)$ refers to the classical Sobolev space of order r on ω; inner products in a function space V are denoted by $(\cdot,\cdot)_V$, whereas $\langle\cdot,\cdot\rangle_{V,V'}$ is a duality pairing between spaces V and V'. The notation $v_{|_\gamma}$ denotes the trace on $\gamma \subseteq \partial\omega$ of a function $v \in \mathrm{H}^1(\omega)$.

2.1. Variational and three-field formulation. Let us consider a connected three-dimensional fracture network Ω given by the union of open planar fractures $\{F_i\}_{i\in\mathcal{J}}$, $\mathcal{J} = (1, ..., I)$, and surrounded by an impervious rock matrix. This means that the flow, modeled by the Darcy law, only occurs along fractures and through fracture intersections. Given two fractures, their closure intersection is called a *trace*, denoted by S_m, $m \in \mathcal{M} = \{1, ..., M\}$. The set of all traces in Ω is $\mathcal{S}$, whereas for $i \in \mathcal{J}$, the subset $\mathcal{S}_i \subset \mathcal{S}$ contains the traces belonging to the ith fracture; the indexes of traces $S_m \in \mathcal{S}_i$ are collected in the index-set $\mathcal{M}_i$. For each $m \in \mathcal{M}$, the set $I_{S_m} = \{\underline{i}, \bar{i}\}$ denotes the indexes of the two fractures intersecting along S_m, with $\underline{i} < \bar{i}$. The boundary of each fracture F_i is denoted by ∂F_i, whereas we denote by $\partial\Omega$ the union of fracture boundaries in the DFN, i.e., $\partial\Omega = \bigcup_{i=1}^{I} \partial F_i$, and it is split into a Dirichlet part Γ_D and a Neumann part Γ_N such that $\partial\Omega = \Gamma_D \cup \Gamma_N$, $\Gamma_D \cap \Gamma_N = \emptyset$ and $|\Gamma_D| > 0$. Similarly, fracture boundaries have a Dirichlet part $\Gamma_{iD} = \Gamma_D \cap \partial F_i$ and a Neumann part $\Gamma_{iN} = \Gamma_N \cap \partial F_i$. Dirichlet and Neumann boundary conditions on $\partial\Omega$ are expressed by functions G_D and G_N, respectively, and their restrictions to ∂F_i are denoted by G_{iD} and G_{iN}.

We are interested in the computation of the hydraulic head H_i on each fracture $F_i \subset \Omega$, given by the sum of pressure and elevation and described by the Darcy law,

$$-\nabla \cdot (\boldsymbol{K}_i \nabla H_i) = Q_i \qquad \text{in } F_i \setminus \mathcal{S}_i, \tag{2.1}$$

$$H_i = G_{iD} \qquad \text{on } \Gamma_{iD}, \tag{2.2}$$

$$\frac{\partial H_i}{\partial \hat{\nu}_{iN}} = G_{iN} \qquad \text{on } \Gamma_{iN}, \tag{2.3}$$

where $\boldsymbol{K}_i$ is a uniformly positive definite tensor representing fracture transmissivity, Q_i is a known source term and $\frac{\partial H_i}{\partial \hat{\nu}_{iN}} = \hat{n}_{iN} \cdot \boldsymbol{K}_i \nabla H_i$ is the hydraulic head conormal derivative along direction $\hat{n}_{iN}$ normal to Γ_{iN}. Let us set on each fracture the function spaces

$$V_i = \mathrm{H}^1_0(F_i) = \left\{ v \in \mathrm{H}^1(F_i) : v_{|\Gamma_{iD}} = 0 \right\} \quad \forall i \in \mathcal{J},$$
$$V_i^D = \mathrm{H}^1_D(F_i) = \left\{ v \in \mathrm{H}^1(F_i) : v_{|\Gamma_{iD}} = G_{iD} \right\} \quad \forall i \in \mathcal{J}$$

and, for each trace $S_m \in \mathcal{S}$, the space $\mathcal{U}^m := \mathrm{H}^{-\frac{1}{2}}(S_m)$ and its dual $\mathcal{U}^{m\prime}$. Assuming for the moment that $\Gamma_{iD} \neq \emptyset$ $\forall i \in \mathcal{J}$, the variational problem describing the distribution

of H in Ω takes the following form: For all $i \in \mathcal{J}$, find $H_i = H_i^0 + \mathcal{R}_i G_{iD}$ with $\mathcal{R}_i G_{iD} \in V_i^D$ a lifting of the Dirichlet boundary condition and $H_i^0 \in V_i$ such that

$$(\boldsymbol{K}_i \nabla H_i^0, \nabla v_i)_{V_i} = (Q_i, v_i)_{V_i} + \sum_{m \in \mathcal{M}_i} \left\langle \left[\!\left[\frac{\partial H_i^0}{\partial \hat{\nu}_i^m} \right]\!\right], v_{|_{S_m}} \right\rangle_{\mathcal{U}^m, \mathcal{U}^{m\prime}} + \left\langle G_{iN}, v_{|_{\Gamma_{iN}}} \right\rangle_{H^{-\frac{1}{2}}(\Gamma_{iN}), H^{\frac{1}{2}}(\Gamma_{iN})} - (\boldsymbol{K}_i \nabla \mathcal{R}_i G_{iD}, \nabla v_i)_{V_i} \quad v_i \in V_i, \tag{2.4}$$

where $\frac{\partial H_i^0}{\partial \hat{\nu}_i^m} = \hat{n}_i^m \cdot \boldsymbol{K}_i \nabla H_i^0$ is the hydraulic head conormal derivative along direction $\hat{n}_i^m$ normal to $S_m \in \mathcal{S}_i$ and $[\![\frac{\partial H_i^0}{\partial \hat{\nu}_i^m}]\!]$ denotes the jump of $\frac{\partial H_i^0}{\partial \hat{\nu}_i^m}$ across S_m.

Coupling conditions at the traces for problems on intersecting fractures are the continuity of the hydraulic head and flux conservation, expressed by

$$H_{\bar{i}|_{S_m}} - H_{\underline{i}|_{S_m}} = 0 \qquad \text{for } \bar{i}, \underline{i} \in I_{S_m} \quad \forall m, \in \mathcal{M} \tag{2.5}$$

$$\left[\!\left[\frac{\partial H_{\bar{i}}}{\partial \hat{\nu}_{\bar{i}}^m} \right]\!\right] + \left[\!\left[\frac{\partial H_{\underline{i}}}{\partial \hat{\nu}_{\underline{i}}^m} \right]\!\right] = 0 \qquad \text{for } \bar{i}, \underline{i} \in I_{S_m} \quad \forall m \in \mathcal{M}. \tag{2.6}$$

Let us introduce on each trace $S_m \in \mathcal{S}$ the space $\mathcal{H}^m = \mathrm{H}^{\frac{1}{2}}(S_m)$ and its dual $\mathcal{H}^{m\prime}$ and the quantities $\Psi^m \in \mathcal{H}^m$ and $\Lambda^m \in \mathcal{U}^m$, representing the unknown value of the hydraulic head on S_m and of the flux jump across S_m, respectively. Then coupling condition (2.5) can be rewritten in a weak form as, $\forall m \in \mathcal{M}$, $\{\underline{i}, \bar{i}\} = I_{S_m}$,

$$\begin{aligned} \left\langle H_{\underline{i}|_{S_m}} - \Psi^m, \mu_m \right\rangle_{\mathcal{H}^m, \mathcal{H}^{m\prime}} = 0 \quad \forall \mu_m \in \mathcal{H}^{m\prime}, \\ \left\langle H_{\bar{i}|_{S_m}} - \Psi^m, \mu_m \right\rangle_{\mathcal{H}^m, \mathcal{H}^{m\prime}} = 0 \quad \forall \mu_m \in \mathcal{H}^{m\prime} \end{aligned} \tag{2.7}$$

and condition (2.6) as, $\forall m \in \mathcal{M}$, $\{\underline{i}, \bar{i}\} = I_{S_m}$,

$$\begin{aligned} \left\langle \left[\!\left[\frac{\partial H_{\underline{i}}}{\partial \hat{\nu}_{\underline{i}}^m} \right]\!\right] - \Lambda^m, \rho_m \right\rangle_{\mathcal{U}^m, \mathcal{U}^{m\prime}} = 0 \quad \forall \rho_m \in \mathcal{U}^{m\prime}, \\ \left\langle \left[\!\left[\frac{\partial H_{\bar{i}}}{\partial \hat{\nu}_{\bar{i}}^m} \right]\!\right] + \Lambda^m, \rho_m \right\rangle_{\mathcal{U}^m, \mathcal{U}^{m\prime}} = 0 \quad \forall \rho_m \in \mathcal{U}^{m\prime}. \end{aligned} \tag{2.8}$$

Assuming, for the sake of simplicity, that homogenous Dirichlet and Neumann boundary conditions are imposed on ∂F_i, $\forall i \in \mathcal{J}$, the three-field formulation [14] of problem (2.4) takes the following form: Find $(H_i, \Lambda^m, \Psi^m) \in V_i \times \mathcal{H}^m \times \mathcal{U}^m$, for all $i \in \mathcal{J}$ and for all $m \in \mathcal{M}_i$ such that

$$(\boldsymbol{K}_i \nabla H_i, \nabla v_i)_{V_i} - \sum_{m \in \mathcal{M}_i} \left\langle (-1)^{\chi_i^m} \Lambda^m, v_{i|_{S_m}} \right\rangle_{\mathcal{U}^m, \mathcal{U}^{m\prime}} = (Q_i, v_i)_{V_i} \qquad \forall v_i \in V_i, \tag{2.9}$$

$$\sum_{j \in I_{S_m}} \left\langle H_{j|_{S_m}} - \Psi^m, \mu_m \right\rangle_{\mathcal{H}^m, \mathcal{H}^{m\prime}} = 0 \qquad \forall \mu_m \in \mathcal{H}^{m\prime}, \tag{2.10}$$

with, for $i \in \mathcal{J}$, $m \in \mathcal{M}_i$, $\chi_i^m = 1$ if $i = \max(I_{S_m})$ and zero otherwise. In (2.9) we have used the property $\mathcal{U}^{m\prime} = \mathcal{H}^m = \mathrm{H}^{\frac{1}{2}}(S_m)$. For a given fracture F_i, the second term in (2.9), $(-1)^{\chi_i^m} \Lambda^m$, represents the flux entering the fracture through its traces. On each trace S_m, $m \in \mathcal{M}$, the flux Λ^m is considered positive for fracture $F_{\underline{i}}$ and

negative for fracture $F_{\bar{i}}$, ensuring the conservation condition. In order to remove the assumption of having a nonempty portion of the Dirichlet boundary on each fracture, (2.9) can be modified as follows: On each fracture F_i, $i \in \mathcal{J}$, and on each trace S_m, $m \in \mathcal{M}_i$, find $(H_i, \Lambda^m, \Psi^m) \in V_i \times \mathcal{H}^m \times \mathcal{U}^m$ such that

(2.11)
$$(\boldsymbol{K}_i \nabla H_i, \nabla v_i)_{V_i} + \sum_{m \in \mathcal{M}_i} \left(\alpha \left(H_{i|_{S_m}}, v_{i|_{S_m}} \right)_{\mathcal{H}^m} - \left\langle (-1)^{\chi_i^m} \Lambda^m, v_{i|_{S_m}} \right\rangle_{\mathcal{U}^m, \mathcal{U}^{m\prime}} \right)$$
$$= \alpha \sum_{m \in \mathcal{M}_i} \left(\Psi^m, v_{i|_{S_m}} \right)_{\mathcal{H}^m} + (Q_i, v_i)_{V_i} \qquad \forall v_i \in V_i,$$

$$\sum_{j \in I_{S_m}} \left\langle H_{j|_{S_m}} - \Psi^m, \mu_m \right\rangle_{\mathcal{H}^m, \mathcal{H}^{m\prime}} = 0 \qquad \forall \mu_m \in \mathcal{H}^{m\prime}, \tag{2.12}$$

which, for $\alpha > 0$, ensures well-posedness of (2.11) even if $\Gamma_{iD} = \emptyset$ for all but one fracture.

2.2. PDE-constrained optimization formulation. The discretization of the continuity condition (2.12) would require some sort of mesh conformity at the traces and a discrete inf-sup condition to have well-posedness of (2.11)–(2.12). We rewrite instead problem (2.11)–(2.12) in a new formulation allowing a discretization on arbitrary meshes, from which a viable and robust numerical scheme can be derived, independently of DFN geometrical complexity. At this aim we transform (2.11)–(2.12) in a PDE-constrained optimization problem, in which a cost functional is introduced in order to enforce the continuity condition on traces. For each fracture F_i and each trace $S_m \in \mathcal{S}_i$, let us introduce the trace operator $\Gamma_i^m : V_i \to \mathcal{H}^m$, $\Gamma_i^m(v_i) = v_{i|_{S_m}}$ $\forall v \in V_i$, and the cost functional

$$J_i^m(H_i, \Lambda^m, \Psi^m) = ||\Gamma_i^m H_i(\Lambda^m, \Psi^m) - \Psi^m||^2_{\mathcal{H}^m}, \tag{2.13}$$

which expresses the error in the fulfillment of continuity at trace S_m. Let us then introduce, for each fracture F_i, $i \in \mathcal{J}$, the spaces

$$\mathcal{H}^{\mathcal{M}_i} = \prod_{m \in \mathcal{M}_i} \mathcal{H}^m, \qquad \mathcal{U}^{\mathcal{M}_i} = \prod_{m \in \mathcal{M}_i} \mathcal{U}^m$$

and the variables

$$\Psi_i = \prod_{m \in \mathcal{M}_i} \Psi^m \in \mathcal{H}^{\mathcal{M}_i}, \qquad \Lambda_i = \prod_{m \in \mathcal{M}_i} \Lambda^m \in \mathcal{U}^{\mathcal{M}_i}.$$

Setting $\Gamma_i = \prod_{m \in \mathcal{M}_i} \Gamma_i^m$, $\Gamma_i : V_i \to \mathcal{H}^{\mathcal{M}_i}$, we define the linear bounded operators $A_i : V_i \to V_i'$, $\mathcal{B}_i : \mathcal{U}^{\mathcal{M}_i} \to V_i'$, $\mathcal{C}_i : \mathcal{H}^{\mathcal{M}_i} \to V_i'$ such that

$$\langle A_i H_i, v_i \rangle_{V_i', V_i} = (\boldsymbol{K}_i \nabla H_i, \nabla v_i)_{V_i} + \alpha (\Gamma_i H_i, \Gamma_i v_i)_{\mathcal{H}^{\mathcal{M}_i}}, \qquad v_i \in V_i, \tag{2.14}$$

$$\langle \mathcal{B}_i \Lambda_i, v_i \rangle_{V_i', V_i} = \left\langle (-1)^{\chi_i^m} \Lambda_i, \Gamma_i v_i \right\rangle_{\mathcal{U}^{\mathcal{M}_i}, \mathcal{U}^{\mathcal{M}_i\prime}}, \qquad v_i \in V_i, \tag{2.15}$$

$$\langle \mathcal{C}_i \Psi_i, v_i \rangle_{V_i', V_i} = \alpha (\Psi_i, \Gamma_i v_i)_{\mathcal{H}^{\mathcal{M}_i}}, \qquad v_i \in V_i, \tag{2.16}$$

and their adjoints $A_i^* : V_i \to V_i'$, $\mathcal{B}_i^* : V_i \to \mathcal{U}^{\mathcal{M}_i\prime}$ and $\mathcal{C}_i^* : V_i \to \mathcal{H}^{\mathcal{M}_i\prime}$. Defining, then, the spaces

$$\mathcal{H} = \prod_{m \in \mathcal{M}} \mathcal{H}^m \qquad \mathcal{U} = \prod_{m \in \mathcal{M}} \mathcal{U}^m$$

and the global control variables

$$\Psi = \prod_{m\in\mathcal{M}} \Psi^m \in \mathcal{H} \qquad \Lambda = \prod_{m\in\mathcal{M}} \Lambda^m \in \mathcal{U},$$

a global functional can be introduced as

$$J(H,\Lambda,\Psi) = \sum_{i\in\mathcal{J}} J_i(H_i,\Lambda_i,\Psi_i) = \sum_{i\in\mathcal{J}}\sum_{m\in\mathcal{M}_i} J_i^m(H_i,\Lambda^m,\Psi^m), \tag{2.17}$$

and problem (2.11)–(2.12) can be written in the form

$$\min_{(\Lambda,\Psi)} \frac{1}{2} J(H,\Lambda,\Psi) \text{ subject to} \tag{2.18}$$
$$A_i H_i - \mathcal{B}_i\Lambda_i - \mathcal{C}_i\Psi_i = Q_i \qquad \forall i \in \mathcal{J},$$

where the scaling factor $\frac{1}{2}$ is introduced for the sake of convenience. The following result characterizes the solution to (2.18).

PROPOSITION 2.1. *The optimal control (Λ,Ψ) providing the solution to (2.18) satisfies, $\forall i \in \mathcal{J}$,*

$$\Theta_{\mathcal{U}^{\mathcal{M}_i}}^{-1} \mathcal{B}_i{}^* P_i = 0, \tag{2.19}$$

$$\Theta_{\mathcal{H}^{\mathcal{M}_i}}^{-1} \mathcal{C}_i{}^* P_i - \Gamma_i H_i(\Lambda_i,\Psi_i) + \Psi_i = 0, \tag{2.20}$$

where $P_i \in V_i$ is the solution of

$$A_i{}^* P_i = \Gamma_i{}^* \Theta_{\mathcal{H}^{\mathcal{M}_i}} (\Gamma_i H_i(\Lambda_i,\Psi_i) - \Psi_i), \tag{2.21}$$

$\Theta_{\mathcal{H}^{\mathcal{M}_i}} : \mathcal{H}^{\mathcal{M}_i} \to \mathcal{H}^{\mathcal{M}_i}{}'$, $\Theta_{\mathcal{U}^{\mathcal{M}_i}} : \mathcal{U}^{\mathcal{M}_i} \to \mathcal{U}^{\mathcal{M}_i}{}'$ are Riesz isomorphisms, and $\Gamma_i^* : \mathcal{H}^{\mathcal{M}_i}{}' \to V_i'$ is the adjoint of operator Γ_i.

Proof. Let us consider the increments $\delta\Lambda_i$ and $\delta\Psi_i$, concerning the control variables Λ_i and Ψ_i, respectively, and let us differentiate the cost functional $J(H,\Lambda,\Psi)$ with respect to the control variables:

$$\begin{aligned}\frac{\partial J_i}{\partial \Lambda_i}(H_i,\Lambda_i+\delta\Lambda_i,\Psi_i) &= 2(\Gamma_i H_i(\Lambda_i,\Psi_i) - \Psi_i, \Gamma_i H_i(\delta\Lambda_i,0)_{\mathcal{H}^{\mathcal{M}_i}}) \\ &= 2\left\langle A_i{}^* P_i, A_i^{-1}\mathcal{B}_i\delta\Lambda_i\right\rangle_{V_i',V_i} = 2(\Theta_{\mathcal{U}^{\mathcal{M}_i}}^{-1}\mathcal{B}_i{}^* P_i, \delta\Lambda_i)_{\mathcal{U}^{\mathcal{M}_i}},\end{aligned}$$

$$\begin{aligned}\frac{\partial J_i}{\partial \Psi_i}(H_i,\Lambda_i,\Psi_i+\delta\Psi_i) &= 2\left(\Gamma_i H_i(\Lambda_i,\Psi_i) - \Psi_i, \Gamma_i H_i(0,\delta\Psi_i) - \delta\Psi_i\right)_{\mathcal{H}^{\mathcal{M}_i}} \\ &= 2\left\langle A_i{}^* P_i, A_i^{-1}\mathcal{C}_i\delta\Psi_i\right\rangle_{V_i',V_i} - 2\left(\Gamma_i H_i(\Lambda_i,\Psi_i) - \Psi_i, \delta\Psi_i\right)_{\mathcal{H}^{\mathcal{M}_i}} \\ &= 2\left(\Theta_{\mathcal{H}^{\mathcal{M}_i}}^{-1}\mathcal{C}_i{}^* P_i - \Gamma_i H_i(\Lambda_i,\Psi_i) + \Psi_i, \delta\Psi_i\right)_{\mathcal{H}^{\mathcal{M}_i}}.\end{aligned}$$

This yields the thesis. ∎

The derivatives computed in the proof of Proposition 2.1 represent the Frechet derivative of the Lagrangian function associated to problem (2.18), for which the variable $P_i \in V_i$ is the Lagrangian multiplier on fracture F_i. The solution to problem (2.18) can then be found by imposing stationarity conditions for the Lagrangian. Nevertheless, as we will show later, when dealing with huge and complex DFNs it might

be computationally more convenient to minimize $J(\Lambda, \Psi)$ using an iterative method, such as the conjugate gradient method. Starting from the derivatives computed in Proposition 2.1, let us consider the following quantities for each $i \in \mathcal{J}$:

$$\delta\Lambda_i = \Theta^{-1}_{\mathcal{U}^{\mathcal{M}_i}} \mathcal{B}_i{}^* P_i, \qquad \delta\Lambda = \sum_{i\in\mathcal{J}} \delta\Lambda_i, \tag{2.22}$$

$$\delta\Psi_i = \Theta^{-1}_{\mathcal{H}^{\mathcal{M}_i}} \mathcal{C}_i{}^* P_i - \Gamma_i H_i(\Lambda_i, \Psi_i) + \Psi_i, \qquad \delta\Psi = \sum_{i\in\mathcal{J}} \delta\Psi_i. \tag{2.23}$$

Let then $\delta H_i = H_i(\delta\Lambda_i, \delta\Psi_i)$ and δP_i be the solutions of

$$A_i \delta H_i = \mathcal{B}_i \delta\Lambda_i + \mathcal{C}_i \delta\Psi_i \quad \forall i \in \mathcal{J}, \tag{2.24}$$

$$A_i{}^* \delta P_i = \Gamma_i{}^* \Theta_{\mathcal{H}^{\mathcal{M}_i}} (\Gamma_i \delta H_i - \delta\Psi_i) \quad \forall i \in \mathcal{J}. \tag{2.25}$$

PROPOSITION 2.2. *Given the control variable $W := (\Lambda, \Psi)$, let us increment it by a step $\zeta\delta W$, with $\delta W := (\delta\Lambda, \delta\Psi)$. The steepest descent method corresponds to the step size*

$$\zeta = -\frac{\sum_{i\in\mathcal{J}} [(\delta\Lambda_i, \delta\Lambda_i)_{\mathcal{U}^{\mathcal{M}_i}} + (\delta\Psi_i, \delta\Psi_i)_{\mathcal{H}^{\mathcal{M}_i}}]}{\sum_{i\in\mathcal{J}} \left[\langle \mathcal{B}_i\delta\Lambda_i + \mathcal{C}_i\delta\Psi_i, \delta P_i\rangle_{V_i', V_i} - (\Gamma_i\delta H_i, \delta\Psi_i)_{\mathcal{H}^{\mathcal{M}_i}} + (\delta\Psi_i, \delta\Psi_i)_{\mathcal{H}^{\mathcal{M}_i}}\right]}. \tag{2.26}$$

Proof. It is sufficient to set to zero the derivative $\frac{\partial J(W+\zeta\delta W)}{\partial\zeta}$,

$$\begin{aligned} J(W + \zeta\delta W) &= J(W) + 2\zeta \sum_{i\in\mathcal{J}} (\Gamma_i H_i(\Lambda_i, \Psi_i) - \Psi_i, \Gamma_i H_i(\delta\Lambda_i, \delta\Psi_i) - \delta\Psi_i)_{\mathcal{H}^{\mathcal{M}_i}} \\ &\quad + \zeta^2 \sum_{i\in\mathcal{J}} ||\Gamma_i H_i(\delta\Lambda_i, \delta\Psi_i) - \delta\Psi_i||^2_{\mathcal{H}^{\mathcal{M}_i}}, \\ \frac{\partial J(W + \zeta\delta W)}{\partial\zeta} &= 2 \sum_{i\in\mathcal{J}} (\Gamma_i H_i(\Lambda_i, \Psi_i) - \Psi_i, \Gamma_i H_i(\delta\Lambda_i, \delta\Psi_i) - \delta\Psi_i)_{\mathcal{H}^{\mathcal{M}_i}} \\ &\quad + 2\zeta \sum_{i\in\mathcal{J}} ||\Gamma_i H_i(\delta\Lambda_i, \delta\Psi_i) - \delta\Psi_i||^2_{\mathcal{H}^{\mathcal{M}_i}} = 0, \\ \zeta &= -\frac{\sum_{i\in\mathcal{J}} (\Gamma_i H_i(\Lambda_i, \Psi_i) - \Psi_i, \Gamma_i H_i(\delta\Lambda_i, \delta\Psi_i) - \delta\Psi_i)_{\mathcal{H}^{\mathcal{M}_i}}}{\sum_{i\in\mathcal{J}} ||\Gamma_i H_i(\delta\Lambda_i, \delta\Psi_i) - \delta\Psi_i||^2_{\mathcal{H}^{\mathcal{M}_i}}}, \end{aligned}$$

from which the thesis follows. ∎

3. Discretization. In this section we introduce suitable space dicretizations on fractures and traces, and we derive the corresponding discrete formulation of the problem. In the following, we will denote by lowercase letters the finite dimensional approximation of the continuous variables. The same notation will be used for the discrete functions and for the corresponding vectors of degrees of freedom (DOFs) with respect to suitable bases, the difference being clear from the context.

Let us build a triangular mesh on each fracture F_i, $i \in \mathcal{J}$, nonconforming to the traces on the fracture, and let us define, on this mesh, suitable finite elements basis functions for the hydraulic head $\{\varphi_{i,k}\}_{k=1,\dots,N_H^i}$, with N_H^i denoting the number of

DOFs on the ith fracture. The approximation of H_i with respect to this basis is

$$h_i = \sum_{k=1}^{N_H^i} h_{i,k}\varphi_{i,k}, \tag{3.1}$$

where $h_{i,k}$ are the values of the DOFs. For each trace $S_m \in \mathcal{S}$, let us build two different meshes for defining the approximation of the two control variables Λ^m and Ψ^m, and let us consider two bases $\{\eta_k^m\}_{k=1,\dots,N_\Lambda^m}$ and $\{\theta_k^m\}_{k=1,\dots,N_\Psi^m}$, with N_Λ^m and N_Ψ^m denoting the number of DOFs on the mth trace, respectively, for Λ^m and Ψ^m. It is worth highlighting that neither a unique discretization nor the same basis is required for the two control variables. The discrete control variables are

$$\lambda^m = \sum_{k=1}^{N_\Lambda^m} \lambda_k^m \eta_k^m, \qquad \psi^m = \sum_{k=1}^{N_\Psi^m} \psi_k^m \theta_k^m, \tag{3.2}$$

with λ_k^m and ψ_k^m denoting the values assigned to the DOFs.

Let us then define, for each fracture F_i, the vector of the hydraulic head DOFs $h_i \in \mathbb{R}^{N_H^i}$ obtained collecting columnwise the relative DOFs and matrix $\boldsymbol{A}_i$ defined as

$$\boldsymbol{A_i} \in \mathbb{R}^{N_H^i \times N_H^i}, \quad (A_i)_{kl} = \int_{F_i} \boldsymbol{K}_i \nabla\varphi_{i,k} \nabla\varphi_{i,l}\, dF_i + \alpha \int_{\mathcal{S}_i} \varphi_{i,k|_{\mathcal{S}_i}} \varphi_{i,l|_{\mathcal{S}_i}}\, dS. \tag{3.3}$$

For each trace $S_m \in \mathcal{S}$, let us consider the vectors of control variable DOFs $\lambda^m \in \mathbb{R}^{N_\Lambda^m}$ and $\psi^m \in \mathbb{R}^{N_\Psi^m}$, obtained once again collecting columnwise the corresponding DOFs. Furthermore, let us introduce the following matrices, defined on each trace S_m of each fracture F_i $\forall i \in \mathcal{J}$ $\forall m \in \mathcal{M}_i$:

$$\boldsymbol{\mathcal{B}_i^m} \in \mathbb{R}^{N_H^i \times N_\Lambda^m}, \quad (\mathcal{B}_i^m)_{kl} = (-1)^{\chi_i^m} \int_{S_m} \varphi_{i,k|_{S_m}}\, \eta_l^m\, dS, \tag{3.4}$$

$$\boldsymbol{\mathcal{C}_i^m} \in \mathbb{R}^{N_H^i \times N_\Psi^m}, \quad (\mathcal{C}_i^m)_{kl} = \alpha \int_{S_m} \varphi_{i,k|_{S_m}}\, \theta_l^m\, dS. \tag{3.5}$$

Let us also introduce the matrices $\boldsymbol{\mathcal{B}_i}$ and $\boldsymbol{\mathcal{C}_i}$ on F_i, obtained collecting, respectively, the matrices $\boldsymbol{\mathcal{B}_i^m}$ and $\boldsymbol{\mathcal{C}_i^m}$ for increasing values of indices $m \in \mathcal{M}_i = (m_1, \dots m_{M_i})$:

$$\boldsymbol{\mathcal{B}_i} = \left[\boldsymbol{\mathcal{B}_i^{m_1}}, \boldsymbol{\mathcal{B}_i^{m_2}}, \dots, \boldsymbol{\mathcal{B}_i^{m_{M_i}}}\right], \qquad \boldsymbol{\mathcal{C}_i} = \left[\boldsymbol{\mathcal{C}_i^{m_1}}, \boldsymbol{\mathcal{C}_i^{m_2}}, \dots, \boldsymbol{\mathcal{C}_i^{m_{M_i}}}\right]. \tag{3.6}$$

Finally, let us define the vectors

$$\lambda_i = \begin{bmatrix} \lambda^{m_1} \\ \lambda^{m_2} \\ \vdots \\ \lambda^{m_{M_i}} \end{bmatrix} \in \mathbb{R}^{N_\Lambda^{\mathcal{M}_i}}, \qquad \psi_i = \begin{bmatrix} \psi^{m_1} \\ \psi^{m_2} \\ \vdots \\ \psi^{m_{M_i}} \end{bmatrix} \in \mathbb{R}^{N_\Psi^{\mathcal{M}_i}}, \tag{3.7}$$

with $N_\Lambda^{\mathcal{M}_i} = \sum_{m\in\mathcal{M}_i} {N_\Lambda}^m$ and $N_\Psi^{\mathcal{M}_i} = \sum_{m\in\mathcal{M}_i} N_\Psi^m$. We are then able to write the discrete matrix formulation of the constraints equation in problem (2.18) as

$$\boldsymbol{A_i} h_i - \boldsymbol{\mathcal{B}_i} \lambda_i - \boldsymbol{\mathcal{C}_i} \psi_i = q_i, \tag{3.8}$$

where $q_i \in \mathbb{R}^{N_H^i}$ corresponds to the discrete source term on F_i.

In view of a global formulation over the whole DFN, a global vector containing the head's DOFs is built as

$$h = \begin{bmatrix} h_1 \\ h_2 \\ \vdots \\ h_I \end{bmatrix} \in \mathbb{R}^{N_H^F}, \tag{3.9}$$

where $N_H = \sum_{i \in \mathcal{J}} N_H^i$. Global vectors for the control variables are obtained concatenating columnwise vectors $\{\lambda^m\}_{m \in \mathcal{M}}$ and $\{\psi^m\}_{m \in \mathcal{M}}$, namely,

$$\lambda = \begin{bmatrix} \lambda^1 \\ \lambda^2 \\ \vdots \\ \lambda^M \end{bmatrix} \in \mathbb{R}^{N_\Lambda}, \qquad \psi = \begin{bmatrix} \psi^1 \\ \psi^2 \\ \vdots \\ \psi^M \end{bmatrix} \in \mathbb{R}^{N_\Psi}, \tag{3.10}$$

where $N_\Lambda = \sum_{m \in \mathcal{M}} N_\Lambda^m$ and $N_\Psi = \sum_{m \in \mathcal{M}} N_\Psi^m$. Let us define, $\forall i \in \mathcal{J}$, matrices

$$\boldsymbol{\mathcal{B}_i^m} = \mathbf{0} \in \mathbb{R}^{N_H^i \times N_\Lambda^m} \ \forall m \notin \mathcal{M}_i, \tag{3.11}$$

$$\boldsymbol{\mathcal{C}_i^m} = \mathbf{0} \in \mathbb{R}^{N_H^i \times N_\Psi^m} \ \forall m \notin \mathcal{M}_i, \tag{3.12}$$

and, recalling definitions (3.4) and (3.5), we build

$$\boldsymbol{\mathcal{B}_i^{\mathcal{M}}} = \left[\boldsymbol{\mathcal{B}_i^1}, \boldsymbol{\mathcal{B}_i^2}, \ldots, \boldsymbol{\mathcal{B}_i^M}\right] \in \mathbb{R}^{N_H^i \times N_\Lambda}, \tag{3.13}$$

$$\boldsymbol{\mathcal{C}_i^{\mathcal{M}}} = \left[\boldsymbol{\mathcal{C}_i^1}, \boldsymbol{\mathcal{C}_i^2}, \ldots, \boldsymbol{\mathcal{C}_i^M}\right] \in \mathbb{R}^{N_H^i \times N_\Lambda}, \tag{3.14}$$

and

$$\boldsymbol{\mathcal{B}} = \begin{bmatrix} \boldsymbol{\mathcal{B}_1^{\mathcal{M}}} \\ \boldsymbol{\mathcal{B}_2^{\mathcal{M}}} \\ \vdots \\ \boldsymbol{\mathcal{B}_I^{\mathcal{M}}} \end{bmatrix} \in \mathbb{R}^{N_H \times N_\Lambda}, \qquad \boldsymbol{\mathcal{C}} = \begin{bmatrix} \boldsymbol{\mathcal{C}_1^{\mathcal{M}}} \\ \boldsymbol{\mathcal{C}_2^{\mathcal{M}}} \\ \vdots \\ \boldsymbol{\mathcal{C}_I^{\mathcal{M}}} \end{bmatrix} \in \mathbb{R}^{N_H \times N_\Psi}, \tag{3.15}$$

such that the global discrete form of the constraints equation becomes

$$\boldsymbol{A}h - \boldsymbol{\mathcal{B}}\lambda - \boldsymbol{\mathcal{C}}\psi = q, \tag{3.16}$$

where $\boldsymbol{A} = \mathrm{diag}(\boldsymbol{A_1}\ \boldsymbol{A_2}\ \ldots\ \boldsymbol{A_I}) \in \mathbb{R}^{N_H \times N_H}$ and $q = (q_1^T\ q_2^T\ \ldots\ q_I^T)^T \in \mathbb{R}^{N_H}$.

The discrete functional is obtained from (2.13) by use of the discrete functions and of L^2 norms in place of $\mathcal{H}^m$ norms, this yielding, for $i \in \mathcal{J}$, $m \in \mathcal{M}_i$,

$$\tilde{J}_i^m(\lambda^m, \psi^m) = ||h_{i|_{S_m}}(\lambda^m, \psi^m) - \psi^m||_{L^2}^2. \tag{3.17}$$

Defining the matrices

$$\boldsymbol{G_i^{h,m}} \in \mathbb{R}^{N_H^i \times N_H^i}, \quad \left(G_i^{h,m}\right)_{kl} = \int_{S_m} \varphi_{i,k|_{S_m}} \varphi_{i,l|_{S_m}}\, dS, \tag{3.18}$$

$$\boldsymbol{G^{\psi,m}} \in \mathbb{R}^{N_\Psi^m \times N_\Psi^m}, \quad \left(G^{\psi,m}\right)_{kl} = \int_{S_m} \theta_k^m \theta_l^m\, dS, \tag{3.19}$$

and

$$\boldsymbol{G_i^h} = \sum_{m \in \mathcal{M}_i} \boldsymbol{G_i^{h,m}} \in \mathbb{R}^{N_H^i \times N_H^i}, \tag{3.20}$$

$$\boldsymbol{G_i^\psi} = \mathrm{diag}(\boldsymbol{G^{\psi,m_1}}\ \boldsymbol{G^{\psi,m_2}}\ \ldots\ \boldsymbol{G^{\psi,m_{M_i}}}) \in \mathbb{R}^{N_\Psi^{\mathcal{M}_i} \times N_\Psi^{\mathcal{M}_i}}, \tag{3.21}$$

the discrete cost functional relative to the ith fracture takes the form

$$\tilde{J}_i(\lambda_i, \psi_i) = h_i^T \boldsymbol{G_i^h} h_i + \psi_i^T \boldsymbol{G_i^\psi} \psi_i - h_i^T \boldsymbol{\mathcal{C}_i} \psi_i - \psi_i^T \boldsymbol{\mathcal{C}_i^T} h_i \quad \forall i \in \mathcal{J}, \tag{3.22}$$

where $h_i = h_i(\lambda_i, \psi_i)$. Finally, introducing the matrices

$$\boldsymbol{G^h} = \mathrm{diag}(\boldsymbol{G_1^h}\ \boldsymbol{G_2^h}\ \ldots\ \boldsymbol{G_I^h}) \in \mathbb{R}^{N_H \times N_H}, \tag{3.23}$$

$$\boldsymbol{G^\psi} = 2\left(\mathrm{diag}(\boldsymbol{G_1^\psi}\ \boldsymbol{G_2^\psi}\ \ldots\ \boldsymbol{G_M^\psi})\right) \in \mathbb{R}^{N_\Psi \times N_\Psi}, \tag{3.24}$$

the global discrete matrix formulation of the cost functional is obtained as

$$\tilde{J}(\lambda, \psi) = h^T \boldsymbol{G^h} h + \psi^T \boldsymbol{G^\psi} \psi - h^T \boldsymbol{\mathcal{C}} \psi - \psi^T \boldsymbol{\mathcal{C}}^T h, \tag{3.25}$$

with $h = h(\lambda, \psi)$, thanks to which we obtain the following global discrete matrix formulation of the problem describing the subsurface flow through a DFN:

$$\min_{(\lambda,\psi)} \frac{1}{2} \tilde{J}(\lambda, \psi) \text{ subject to (3.16)}. \tag{3.26}$$

Exploiting the linearity of the constraints, we derive an unconstrained minimization problem equivalent to (3.26): Replacing $h = h(\lambda, \psi) = \boldsymbol{A}^{-1}\boldsymbol{\mathcal{B}}\lambda + \boldsymbol{A}^{-1}\boldsymbol{\mathcal{C}}\psi + \boldsymbol{A}^{-1}q$ in (3.25), we rewrite (3.26) as

$$\min_{(\lambda,\psi)} \frac{1}{2} \tilde{J}^*(\lambda, \psi), \tag{3.27}$$

where

$$\tilde{J}^*(\lambda, \psi) = \begin{bmatrix} \lambda^T & \psi^T \end{bmatrix} \hat{\boldsymbol{G}} \begin{bmatrix} \lambda \\ \psi \end{bmatrix} + 2d^T \begin{bmatrix} \lambda \\ \psi \end{bmatrix} + q^T \left[\boldsymbol{A}^{-T} \boldsymbol{G^h} \boldsymbol{A}^{-1}\right] q, \tag{3.28}$$

with

$$\hat{\boldsymbol{G}} = \begin{bmatrix} \boldsymbol{\mathcal{B}}^T \boldsymbol{A}^{-T} \boldsymbol{G^h} \boldsymbol{A}^{-1} \boldsymbol{\mathcal{B}} & \boldsymbol{\mathcal{B}}^T \boldsymbol{A}^{-T} (\boldsymbol{G^h} \boldsymbol{A}^{-1} - \boldsymbol{I}) \boldsymbol{\mathcal{C}} \\ \boldsymbol{\mathcal{C}}^T (\boldsymbol{A}^{-T} \boldsymbol{G^h} - \boldsymbol{I}) \boldsymbol{A}^{-1} \boldsymbol{\mathcal{B}} & \boldsymbol{G^\psi} + \boldsymbol{\mathcal{C}}^T (\boldsymbol{A}^{-T} \boldsymbol{G^h} \boldsymbol{A}^{-1} - \boldsymbol{A}^{-T} - \boldsymbol{A}^{-1}) \boldsymbol{\mathcal{C}} \end{bmatrix} \tag{3.29}$$

and

$$d^T = q^T [\boldsymbol{A}^{-T} \boldsymbol{G^h} \boldsymbol{A}^{-1} \boldsymbol{\mathcal{B}} \quad \boldsymbol{A}^{-T} (\boldsymbol{G^h} \boldsymbol{A}^{-1} - \boldsymbol{I}) \boldsymbol{\mathcal{C}}]. \tag{3.30}$$

4. Existence and uniqueness of the discrete solution. The system of optimality conditions (cKKT conditions) for problem (3.26) can be written as

$$\begin{bmatrix} \boldsymbol{G^h} & 0 & -\boldsymbol{\mathcal{C}} & \boldsymbol{A}^T \\ 0 & 0 & 0 & -\boldsymbol{\mathcal{B}}^T \\ -\boldsymbol{\mathcal{C}}^T & 0 & \boldsymbol{G^\psi} & -\boldsymbol{\mathcal{C}}^T \\ \boldsymbol{A} & -\boldsymbol{\mathcal{B}} & -\boldsymbol{\mathcal{C}} & 0 \end{bmatrix} \begin{bmatrix} h \\ \lambda \\ \psi \\ -p \end{bmatrix} = \begin{bmatrix} 0 \\ 0 \\ 0 \\ q \end{bmatrix}, \tag{4.1}$$

where p is the array of Lagrange multipliers. Grouping matrices and vectors as

$$\boldsymbol{\mathcal{G}} = \begin{bmatrix} \boldsymbol{G^h} & 0 & -\boldsymbol{\mathcal{C}} \\ 0 & 0 & 0 \\ -\boldsymbol{\mathcal{C}}^T & 0 & \boldsymbol{G^\psi} \end{bmatrix}, \quad \boldsymbol{\mathcal{A}} = \begin{bmatrix} \boldsymbol{A} & -\boldsymbol{\mathcal{B}} & -\boldsymbol{\mathcal{C}} \end{bmatrix}, \quad x = \begin{bmatrix} h \\ \lambda \\ \psi \\ -p \end{bmatrix}, \quad q_{\mathrm{KKT}} = \begin{bmatrix} 0 \\ 0 \\ 0 \\ q \end{bmatrix}, \tag{4.2}$$

the KKT system can be compactly rewritten as

$$\boldsymbol{M}_{\mathrm{KKT}} = \begin{bmatrix} \boldsymbol{\mathcal{G}} & \boldsymbol{\mathcal{A}}^T \\ \boldsymbol{\mathcal{A}} & \boldsymbol{O} \end{bmatrix}, \qquad \boldsymbol{M}_{\mathrm{KKT}} x = q_{\mathrm{KKT}}. \tag{4.3}$$

PROPOSITION 4.1. *Matrix $\boldsymbol{M}_{KKT}$ in* (4.3) *is nonsingular, and the unique solution of problem* (4.3) *is equivalent to the solution of* (3.26).

The proof of Proposition 4.1 is based on the following lemma.

LEMMA 4.2. *Let matrices $\boldsymbol{\mathcal{A}}$ and $\boldsymbol{\mathcal{G}}$ be defined as in* (4.2). *Then matrix $\boldsymbol{\mathcal{A}}$ is full rank, and matrix $\boldsymbol{\mathcal{G}}$ is symmetric positive definite on* $\ker(\boldsymbol{\mathcal{A}})$.

Proof. Matrix $\boldsymbol{\mathcal{A}}$ is full rank by construction, as matrix $\boldsymbol{A}$ in (4.2) is nonsingular. The dimension of $\ker(\boldsymbol{\mathcal{A}})$ is thus $N_\Lambda + N_\Psi$. Note that matrix $\boldsymbol{\mathcal{G}}$ is symmetric positive semidefinite by construction. As such, for any vector $y \in \mathbb{R}^{N_H+N_\Lambda+N_\Psi}$, one has $y^T\boldsymbol{\mathcal{G}}y \geq 0$ and $y^T\boldsymbol{\mathcal{G}}y = 0$ if and only if $y \in \ker(\boldsymbol{\mathcal{G}})$. In order to show that $\boldsymbol{\mathcal{G}}$ is positive definite on $\ker(\boldsymbol{\mathcal{A}})$, it suffices to show that $\ker(\boldsymbol{\mathcal{G}}) \cap \ker(\boldsymbol{\mathcal{A}}) = \{0\}$.

Let us consider the canonical basis for $\mathbb{R}^{N_\Lambda+N_\Psi}$ and let e_k denote the kth element of such basis, $k = 1, \ldots, N_\Lambda + N_\Psi$. Let $z_k \in \ker(\boldsymbol{\mathcal{A}})$ be defined as

$$z_k = \begin{bmatrix} \boldsymbol{A}^{-1} \begin{bmatrix} \boldsymbol{\mathcal{B}} & \boldsymbol{\mathcal{C}} \end{bmatrix} e_k \\ e_k \end{bmatrix}.$$

Let us first choose $1 \leq k \leq N_\Lambda$, thus giving

$$z_k = \begin{bmatrix} \boldsymbol{A}^{-1}\boldsymbol{\mathcal{B}}e_k \\ e_k \end{bmatrix} := \begin{bmatrix} \bar{h}_k \\ e_k \end{bmatrix}.$$

Vector $\bar{h}_k$ is different from zero on at least one trace of the network, in virtue of equation (3.8), given the nonsingularity of $\boldsymbol{A}$ and being $\mathcal{B}e_k \neq 0$. Thus, it can be easily concluded that $z_k^T\boldsymbol{\mathcal{G}}z_k = \bar{h}_k^T\boldsymbol{G^h}\bar{h}_k > 0$ for all $1 \leq k \leq N_\Lambda$.

If $N_\Lambda + 1 \leq k \leq N_\Psi$, we have

$$z_k = \begin{bmatrix} \boldsymbol{A}^{-1}\boldsymbol{\mathcal{C}}e_k \\ e_k \end{bmatrix} := \begin{bmatrix} \bar{\bar{h}}_k \\ e_k \end{bmatrix},$$

and, correspondingly to e_k, there is a unique index $m^* \in \mathcal{M}$ such that $\psi^{m^*} \neq 0$, being instead $\lambda \equiv 0$. Let us select the two fractures F_i and F_j such that $\{i, j\} = I_{S_{m^*}}$. If the network contains more than two fractures, at least one of these fractures, say, F_i, has more than one trace, and on F_i the discrete constraint equation reads, $\forall j = 1, \ldots, N_H^i$,

$$\int_{F_i} \boldsymbol{K}_i \nabla\bar{\bar{h}}_k \nabla\varphi_j \, dF_i + \alpha \sum_{\substack{m\in\mathcal{M}_i, \\ m\neq m^*}} \int_{S_m} \bar{\bar{h}}_{k|S_m}\varphi_{j|S_m} \, dS = \alpha \int_{S_{m^*}} \left(\bar{\bar{h}}_{k|S_{m^*}} - \psi^{m^*}\right)\varphi_{j|S_m} \, dS.$$

If we assume $\bar{\bar{h}}_{k|S_{m^*}} = \psi^m \neq 0$, we obtain from the constraint equation $\bar{\bar{h}}_k = 0$, which is absurd. If there are only two fractures in the network, a similar conclusion can be

derived since at least one of the two fractures has a nonempty portion of the Dirichlet boundary. Then we have $z_k^T \boldsymbol{\mathcal{G}} z_k \geq \|\bar{\bar{h}}_{k|S_{m^*}} - \psi^m\|^2 > 0$ for all $N_\Lambda + 1 \leq k \leq N_\Psi$.

Thus, we have proved that, for any $k = 1, \ldots, N_\Lambda + N_\Psi$, $z_k \notin \ker(\boldsymbol{\mathcal{G}})$, and the vector space $\ker(\boldsymbol{\mathcal{A}}) = \text{span}\{z_1, \ldots, z_{N_\Lambda + N_\Psi}\}$ is a subspace of $\text{Im}(\boldsymbol{\mathcal{G}})$. Thus, we have $\ker(\boldsymbol{\mathcal{G}}) \cap \ker(\boldsymbol{\mathcal{A}}) = \{0\}$, which completes the proof. ∎

The proof of Proposition 4.1 follows from Lemma 4.2 using classical arguments (see, e.g., [4, Theorem 3.2]). Note that by the uniqueness of the solution to (3.26) and the problem's equivalence with (3.27), it follows that matrix $\hat{\boldsymbol{G}}$, defined in (3.29), is symmetric positive definite.

5. Problem resolution. Solving the KKT system (4.1) with a direct method in order to compute an approximation of the hydraulic head in Ω might not be a viable option for large networks, for which matrix $\boldsymbol{M}_{\text{KKT}}$ would be extremely large and is likely to be ill-conditioned. Let us then rewrite the cost functional (3.28) in compact form as

$$\tilde{J}^* = w^T \hat{\boldsymbol{G}} w + 2 d^T w + q^T \left[\boldsymbol{A}^{-T} \boldsymbol{G}^{\boldsymbol{h}} \boldsymbol{A}^{-1}\right] q, \tag{5.1}$$

where $w = [\lambda^T, \psi^T]^T$. Note that $\tilde{J}^*$ is a convex functional, whose unique global minimum corresponds to the solution of the linear system $\nabla \tilde{J}^* = \hat{\boldsymbol{G}} w + d = 0$. As an alternative approach, we then solve the unconstrained minimization problem (3.27) via a gradient method, which also results in an algorithm well suited for parallel implementation on parallel computing machines.

Algorithm 5.1 Preconditioned conjugate gradient method applied to $\hat{\boldsymbol{G}} w + d = 0$.

1: Guess $w_0 = [\lambda_0^T, \psi_0^T]^T$
2: $r_0 = \hat{\boldsymbol{G}} w_0 + d$
3: solve $\boldsymbol{P} z_0 = r_0$
4: set $\delta w_0 = -z_0$ and $k = 0$;
5: **while** $\|r_k\| > 0$ **do**
6: $\quad \zeta_k = \dfrac{r_k^T z_k}{\delta w_k^T \hat{\boldsymbol{G}} \delta w_k}$;
7: $\quad w_{k+1} = w_k + \zeta_k \delta w_k$;
8: $\quad r_{k+1} = r_k + \zeta_k \hat{\boldsymbol{G}} \delta w_k$;
9: $\quad$ solve $\boldsymbol{P} z_{k+1} = r_{k+1}$;
10: $\quad \beta_{k+1} = \dfrac{r_{k+1}^T z_{k+1}}{r_k^T z_k}$;
11: $\quad \delta w_{k+1} = -z_{k+1} + \beta_{k+1} \delta w_k$;
12: $\quad k = k + 1$;
13: **end while**

Algorithm 5.1 reports the steps of the application of the preconditioned conjugate gradient scheme to the resolution of $\hat{\boldsymbol{G}} w + d = 0$, with a preconditioner $\boldsymbol{P}$. It is to remark that, for any vector $w = \left[\lambda^T, \psi^T\right]^T$, $\lambda \in \mathbb{R}^{N_\Lambda}$, $\psi \in \mathbb{R}^{N_\Psi}$, the computation of $\hat{\boldsymbol{G}} w$, as at steps 6, 8 of Algorithm 5.1, does not require the inversion of matrix $\boldsymbol{A}$. In particular, it only involves the resolution of linear systems defined independently on each fracture in Ω, which, therefore, can be performed in parallel. Indeed, setting

$$h = \boldsymbol{A}^{-1}(\boldsymbol{\mathcal{B}} \lambda + \boldsymbol{\mathcal{C}} \psi), \qquad p = \boldsymbol{A}^{-T}(\boldsymbol{G}^{\boldsymbol{h}} h - \boldsymbol{\mathcal{C}} \psi),$$

TABLE 1
Geometrical details of the considered networks.

	Fractures	Traces	Traces per fracture		
			Average	Min	Max
DFN3	3	3	2	2	2
DFN10	10	14	2.8	1	5
DFN395	395	629	3.18	1	19

which can be computed locally on the fractures thanks to the structure of the involved matrices, we have

$$\hat{\boldsymbol{G}}w = \begin{bmatrix} \boldsymbol{\mathcal{B}}^T h \\ \boldsymbol{G}^{\boldsymbol{\psi}}\psi + \boldsymbol{\mathcal{C}}^{\boldsymbol{T}} p - \boldsymbol{\mathcal{C}}^T h \end{bmatrix}.$$

The choice of preconditioner $\boldsymbol{P}$ is of great importance for the performance of the method. Given the structure of matrix $\hat{\boldsymbol{G}}$ in (3.29), neglecting off-diagonal terms and simplifying the structure of the bottom-right term, a possible choice is

$$\boldsymbol{P_f} = \begin{bmatrix} \boldsymbol{\mathcal{B}}^T \boldsymbol{A}^{-T} \boldsymbol{G^h} \boldsymbol{A}^{-1} \boldsymbol{\mathcal{B}} & \boldsymbol{O} \\ \boldsymbol{O} & \boldsymbol{G^{\psi}} \end{bmatrix}, \tag{5.2}$$

which provides very good results, as shown in the following section. Unfortunately, the efficient, parallel application of such preconditioner, such as at step 9 of Algorithm 5.1, would require inner loops of a gradient-based scheme, analogously to what was done to solve the main problem. For this reason a new preconditioner is introduced by further simplifying the structure of $\hat{\boldsymbol{G}}$, while preconditioner $\boldsymbol{P_f}$ is used only as a term of comparison. The new preconditioner is defined only extracting M block-diagonal terms of size N_Λ^m, $m = 1, \dots, M$, from matrix $\boldsymbol{\mathcal{D}} := \boldsymbol{\mathcal{B}}^T \boldsymbol{A}^{-T} \boldsymbol{G^h} \boldsymbol{A}^{-1} \boldsymbol{\mathcal{B}}$: Denoting by $N_\Lambda^{[m]} = \sum_{\ell=1}^{m} N_\Lambda^\ell$, matrix $\boldsymbol{\mathcal{D}_m}$ is obtained taking the elements at rows and columns $N_\Lambda^{[m-1]}, \dots, N_\Lambda^{[m]}$ of $\boldsymbol{\mathcal{D}}$, and we then define

$$\boldsymbol{P_d} = \begin{bmatrix} \mathrm{diag}(\boldsymbol{\mathcal{D}_1}, \dots, \boldsymbol{\mathcal{D}_M}) & \boldsymbol{O} \\ \boldsymbol{O} & \boldsymbol{G^{\psi}} \end{bmatrix}. \tag{5.3}$$

6. Numerical results. Here some numerical results are reported to describe the behavior of the proposed numerical method. Three different networks of increasing complexity are considered. First, the hydraulic head is computed on a small network of three fractures, comparing the obtained solution to the available known exact solution. Second, a slightly bigger network of 10 fractures is analyzed in order to highlight and discuss the characteristics of the method in a more realistic yet synthetic, framework. Finally, some results are presented on a complex network counting slightly less than 400 fractures, obtained starting from realistic input data. More details on the networks used in the simulations are reported in Table 1.

First-order Lagrangian finite elements are used to describe the hydraulic head on the fractures, on meshes of triangular elements nonconforming to the traces and independently built on each fracture. Additional enrichment functions are used on the elements intersected by the traces, according to the extended finite element method (XFEM) (see [9]), in order to reproduce jumps of the conormal derivative at fracture intersections on the nonconforming mesh. On each trace S_m, $m \in \mathcal{M}$, a mesh is defined, and piecewise constant basis functions are used for the discretization of control variables Λ^m, and, independently, another mesh is introduced, and piecewise linear

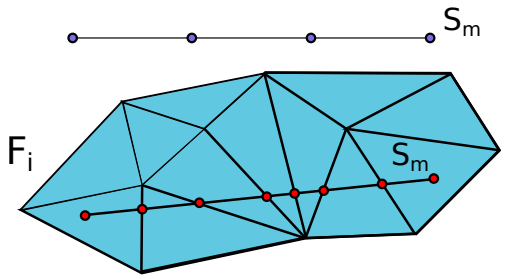

FIG. 1. *Description of parameters* $\boldsymbol{\delta_\lambda}$ *and* $\boldsymbol{\delta_\psi}$. *Red dots mark induced mesh nodes, violet dots mark equally spaced mesh nodes for* Λ *or* Ψ. *The figure refers to* $\boldsymbol{\delta_\lambda} = 0.5$. *Only one fracture is shown for clarity.*

continuous basis functions are used for functions Ψ^m. Clearly, different choices for the basis functions of the various variables are possible, the proposed ones being the more natural given the expected regularity of the solution. We should remark that the flexibility and robustness in handling nonconforming and independently built discretizations on each fracture and on each trace of the network, for each of the variables involved, is a key aspect of the method, which allows one to easily deal with arbitrarily complex geometries without any need of geometrical modification of the DFN.

The size of the triangular mesh on each fracture is expressed by means of a grid parameter $\boldsymbol{\delta_h}$, expressing the maximum element area of mesh elements requested on each fracture. Clearly, a different grid parameter could be used on each fracture, even if here, for simplicity, a single value is adopted. The mesh size on the traces is controlled by two parameters $\boldsymbol{\delta_\lambda}$ and $\boldsymbol{\delta_\psi}$ representing the ratio between the number of mesh elements on the traces, for Λ and Ψ, respectively, and the average number of elements of the mesh induced by the intersection of the trace with the edges of the triangular meshes on each intersecting fracture. A sketch is represented in Figure 1, where the induced mesh nodes on one of the intersecting fractures are depicted with red dots and the equally spaced mesh nodes, e.g., for Λ, with violet dots, corresponding to a value of $\boldsymbol{\delta_\lambda} = 0.5$. Unique values are used for $\boldsymbol{\delta_\lambda}$ and $\boldsymbol{\delta_\psi}$ for all the traces in the network, but different choices are possible.

6.1. DFN3 problem. Let us consider the connected domain Ω shown in Figure 2, given by the union of three planar fractures defined by

$$
\begin{aligned}
F_1 &= \left\{(x,y,z) \in \mathbb{R}^3 : -1 \le x \le 1/2,\ -1 \le y \le 1,\ z = 0\right\},\\
F_2 &= \left\{(x,y,z) \in \mathbb{R}^3 : -1 \le x \le 0,\ y = 0,\ -1 \le z \le 1\right\},\\
F_3 &= \left\{(x,y,z) \in \mathbb{R}^3 : x = -1/2,\ -1 \le y \le 1,\ -1 \le z \le 1\right\},
\end{aligned}
$$

which intersect forming three traces: $S_1 = F_1 \cap F_2$, $S_2 = F_1 \cap F_3$, and $S_3 = F_2 \cap F_3$. This problem is labeled DFN3. The known hydraulic head distribution H^{ex} in Ω is given by

$$
H_1^{\text{ex}}(x,y) = \frac{1}{10}\left(-x - \frac{1}{2}\right)\left(8xy(x^2+y^2)\text{atan2}(y,x) + x^3\right), \tag{6.1}
$$

$$
H_2^{\text{ex}}(x,z) = \frac{1}{10}\left(-x - \frac{1}{2}\right)x^3 - \frac{4}{5}\pi\left(-x - \frac{1}{2}\right)x^3|z|, \tag{6.2}
$$

$$
H_3^{\text{ex}}(y,z) = (y-1)y(y+1)(z-1)z, \tag{6.3}
$$

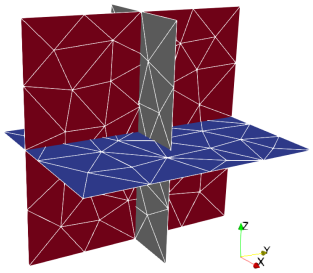

FIG. 2. *DFN3: DFN configuration.*

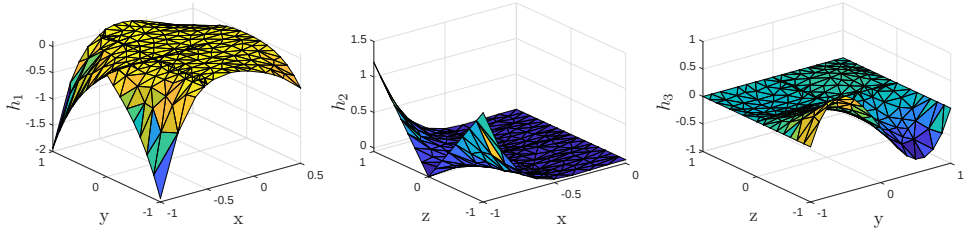

FIG. 3. *DFN3: hydraulic head computed on the fractures. Parameters:* $\boldsymbol{\delta_h} = 0.020$, $\boldsymbol{\delta_\lambda} = 0.5$, $\boldsymbol{\delta_\psi} = 0.3$.

where $\text{atan2}(y, x)$ is the four-quadrant inverse tangent function and is the solution of the problem

$$\begin{aligned} -\nabla \cdot (\nabla H) &= -\nabla \cdot (\nabla H^{\text{ex}}) && \text{in } \Omega \setminus \mathcal{S}, \\ H_{|\partial\Omega} &= H^{\text{ex}}_{|\partial\Omega} && \text{on } \partial\Omega, \end{aligned}$$

with additional conditions of continuity and flux conservation at the traces.

Given the small size of the network, the discrete solution is obtained solving the KKT system (4.1). Five different meshes with an increasing number of elements are considered for the hydraulic head on the fractures, with the mesh parameter $\boldsymbol{\delta_h}$ ranging between 0.02 and 8×10^{-5}, and nine values of $\boldsymbol{\delta_\lambda}$ and $\boldsymbol{\delta_\psi}$ are used, both ranging between 0.1 and 0.9. The coarsest computational mesh on the fractures is reported in Figure 2, highlighting the nonconformity at fracture intersections. An example solution on the three fractures is reported in Figure 3 for mesh parameters $\boldsymbol{\delta_h} = 0.020$, $\boldsymbol{\delta_\lambda} = 0.5$, and $\boldsymbol{\delta_\psi} = 0.3$ showing the irregular behavior of the solution across the trace. The use of the XFEM allows one to correctly reproduce the jumps of the gradient in the direction normal to the traces even if traces arbitrarily cross mesh elements.

We computed errors $\mathcal{E}^h_{L^2}$ and $\mathcal{E}^h_{H^1}$ measuring the $L^2(\Omega)$ and $H^1(\Omega)$ norms, respectively, of the relative difference between the numerical and analytical solution for the hydraulic head on the fractures. Error $\mathcal{E}^\lambda_{L^2}$ is also computed, expressing the $L^2(\mathcal{S})$ norm of the relative difference between the analytical jump of the fluxes at the traces and the computed value of λ. The other mesh parameters are fixed with values $\boldsymbol{\delta_\lambda} = 0.5$ and $\boldsymbol{\delta_\psi} = 0.3$. Let us recall that these parameters represent the ratio between the number of mesh elements on the traces and the number of elements induced by the intersection between the trace and the triangular mesh, so fixing a value does not avoid mesh refinement on traces as a consequence of a refinement on the fractures.

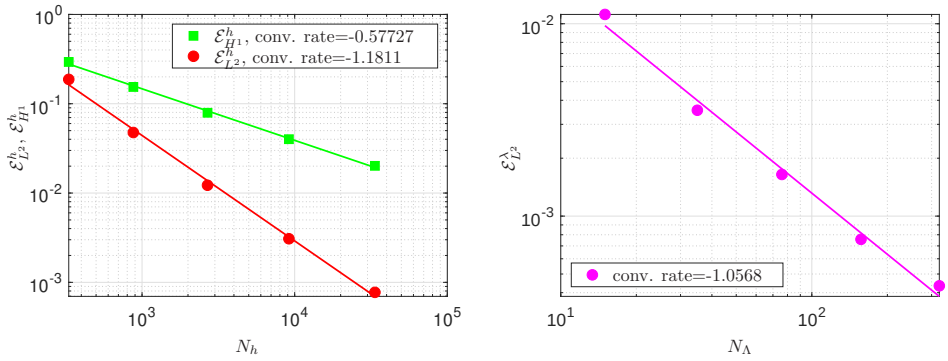

FIG. 4. *DFN3. Left:* $\mathcal{E}^h_{L^2}$ *and* $\mathcal{E}^h_{H^1}$ *versus number of fracture DOFs. Right:* $\mathcal{E}^\lambda_{L^2}$ *versus number of trace DOFs. Other parameters:* $\boldsymbol{\delta_\lambda} = 0.5$, $\boldsymbol{\delta_\psi} = 0.3$.

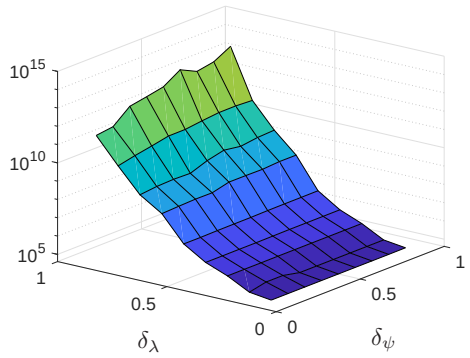

FIG. 5. *DFN3: condition number of the matrix* $\boldsymbol{M}_{KKT}$ *versus* $\boldsymbol{\delta_\lambda}$ *and* $\boldsymbol{\delta_\psi}$. $\boldsymbol{\delta_h} = 0.020$.

The behavior of the errors is reported in Figure 4: $\mathcal{E}^h_{L^2}$ and $\mathcal{E}^h_{H^1}$ are shown on the left, and $\mathcal{E}^\lambda_{L^2}$ is shown on the right, in both cases versus the corresponding number of DOFs. The expected convergence trend is obtained for $\mathcal{E}^h_{L^2}$ and $\mathcal{E}^h_{H^1}$, despite the nonconforming mesh, thanks to the use of the XFEM, and the expected convergence trend is obtained also for $\mathcal{E}^\lambda_{L^2}$.

The effect of the choice of parameters $\boldsymbol{\delta_\lambda}$ and $\boldsymbol{\delta_\psi}$ is also investigated in terms of their influence on the conditioning of the KKT system and on the accuracy of the solution. Figure 5 shows the norm-1 condition number of the KKT matrix for different values of $\boldsymbol{\delta_\lambda}$ and $\boldsymbol{\delta_\psi}$, both ranging between 0.1 and 0.9. System conditioning appears to be more affected by parameter $\boldsymbol{\delta_\lambda}$, whereas its dependence on $\boldsymbol{\delta_\psi}$ is almost negligible, especially for the smaller values $\boldsymbol{\delta_\lambda}$. Figures 6–8 show how parameters $\boldsymbol{\delta_\lambda}$ and $\boldsymbol{\delta_\psi}$ impact the quality of the obtained solution for two different values of $\boldsymbol{\delta_h}$: $\boldsymbol{\delta_h} = 0.020$ on the left and $\boldsymbol{\delta_h} = 0.005$ on the right for all the figures. Figure 6 reports the behavior of error $\mathcal{E}^h_{H^1}$, which appears to be weakly affected by variations of both parameters; a slightly more marked impact of $\boldsymbol{\delta_\lambda}$ is observed on the coarsest mesh with a minimum of $\mathcal{E}^h_{H^1}$ for $\boldsymbol{\delta_\lambda}$ around 0.5. This is motivated by the fact that low values of $\boldsymbol{\delta_\lambda}$ provide a poor approximation of the flux on the traces, which has a detrimental impact on the solution, whereas when $\boldsymbol{\delta_\lambda}$ approaches 0.9, the solution is affected by the higher conditioning of the system. In Figure 7 the trend of error

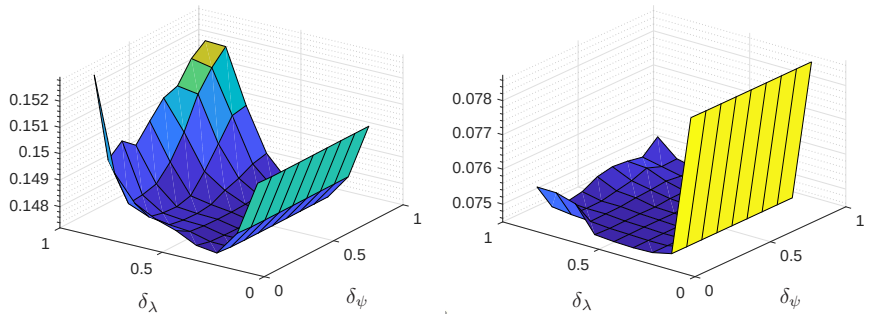

FIG. 6. *DFN3: error* $\mathcal{E}^h_{H^1}$ *versus* $\boldsymbol{\delta_\lambda}$ *and* $\boldsymbol{\delta_\psi}$. *Left:* $\boldsymbol{\delta_h} = 0.020$*; right:* $\boldsymbol{\delta_h} = 0.005$.

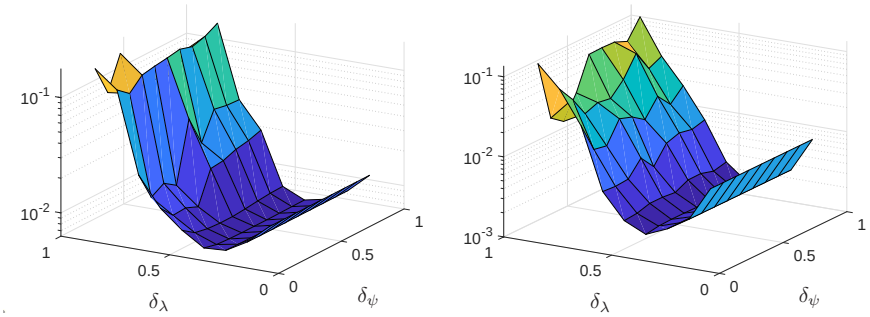

FIG. 7. *DFN3: error* $\mathcal{E}^\lambda_{L^2}$ *versus* $\boldsymbol{\delta_\lambda}$ *and* $\boldsymbol{\delta_\psi}$. *Left:* $\boldsymbol{\delta_h} = 0.020$*; right:* $\boldsymbol{\delta_h} = 0.005$.

$\mathcal{E}^\lambda_{L^2}$ is described, highlighting, as expected, a stronger dependence of this error on $\boldsymbol{\delta_\lambda}$ and also an almost independence from $\boldsymbol{\delta_\psi}$. Again, a minimum of $\mathcal{E}^\lambda_{L^2}$ is observed for values of $\boldsymbol{\delta_\lambda}$ around 0.5, probably again for the effects of system conditioning at the higher values of this parameter. The quantity $\Delta^h_{\mathcal{S}}$ is now introduced to measure the quality of the hydraulic head solution on the traces, defined as

$$\Delta^h_{\mathcal{S}} = \frac{\sqrt{\sum_{m\in\mathcal{M}} ||h_i - h_j||^2_{L^2(S_m)}}}{h_{\max}\sqrt{l_{\text{tot}}}}, \quad i,j \in I_{S_m}, \tag{6.4}$$

where $h_{\max}$ is the maximum value of the hydraulic head in Ω and l_{tot} is the total trace length. Recalling that the continuity of the solution at the traces is enforced through the minimization of functional (3.22) by means of the control variable ψ, the quantity $\Delta^h_{\mathcal{S}}$ is an error indicator on the actual continuity achieved by the method across the traces. Local flux conservation at the traces is instead intrinsically enforced by the method through the definition of a unique variable for flux jump on the two fractures meeting at each trace. In Figure 8 the behavior of $\Delta^h_{\mathcal{S}}$ is reported. A strong influence of $\boldsymbol{\delta_\lambda}$ is again noticed, whereas $\boldsymbol{\delta_\psi}$ has a minor effect, more evident at high values of $\boldsymbol{\delta_\lambda}$. In this case higher values of the parameters provide, in general, lower values of $\Delta^h_{\mathcal{S}}$. Finally, comparing the left and the right pictures of Figures 6–8, we can see that a reduction of the errors and of the error indicator is obtained through mesh refinement.

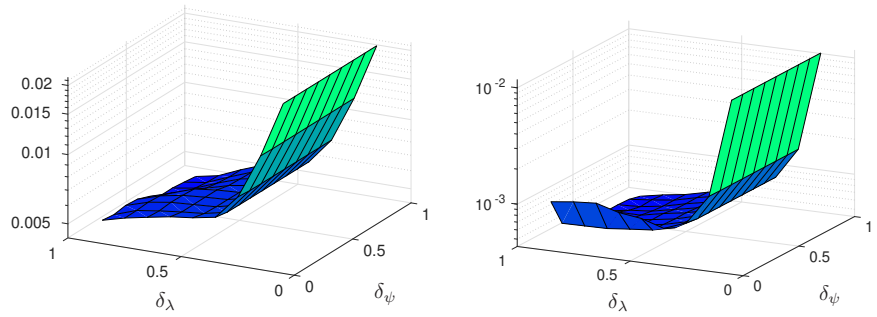

FIG. 8. *DFN3: error indicator* $\Delta_{\mathcal{S}}^h$ *versus* $\boldsymbol{\delta_\lambda}$ *and* $\boldsymbol{\delta_\psi}$*. Left:* $\boldsymbol{\delta_h} = 0.020$*; right:* $\boldsymbol{\delta_h} = 0.005$.

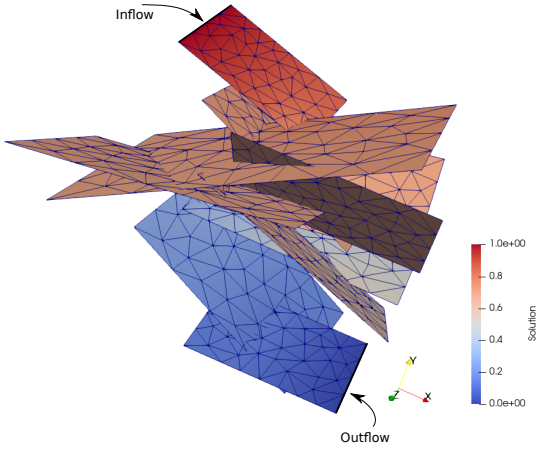

FIG. 9. *DFN10: DFN configuration.*

The effects of ill-conditioning of the KKT system matrix are actually mitigated by solving the problem via the PCG solver in Algorithm 5.1, which is actually an application of the null-space method proposed in [30] to the saddle-point problem (4.1).

6.2. DFN10 problem. A slightly more complex network made of 10 fractures and 14 traces is now considered, as shown in Figure 9 and labeled DFN10. The DFN problem is solved on this network using a uniform unitary value of transmissivity for all fractures and with a prescribed unitary head drop between two selected fracture edges, as marked in Figure 9, and homogeneous Neumann boundary conditions on all other edges. These boundary conditions allow one to identify an inflow and an outflow portion of the boundary, as it usually happens in realistic configurations.

An example solution, obtained with the PCG solver, is reported in Figure 9, along with the nonconforming computational mesh, obtained with $\boldsymbol{\delta_h} = 0.003$, $\boldsymbol{\delta_\lambda} = 0.5$, $\boldsymbol{\delta_\psi} = 0.3$. Figure 10 shows the behavior of the error indicator $\Delta_{\mathcal{S}}^h$ when varying $\boldsymbol{\delta_\lambda}$ and $\boldsymbol{\delta_\psi}$, on two different meshes: a coarse mesh on the left, with $\boldsymbol{\delta_h} = 0.003$, and a fine mesh on the right, with $\boldsymbol{\delta_h} = 7.3 \times 10^{-4}$. As previously noted, the quantity $\Delta_{\mathcal{S}}^h$ is primarily sensible to variations of parameter $\boldsymbol{\delta_\lambda}$, with a decreasing trend for increasing values of $\boldsymbol{\delta_\lambda}$. Parameter $\boldsymbol{\delta_\psi}$ has a minor effect, with a decreasing trend for increasing values of $\boldsymbol{\delta_\psi}$, more relevant at the higher values of $\boldsymbol{\delta_\lambda}$.

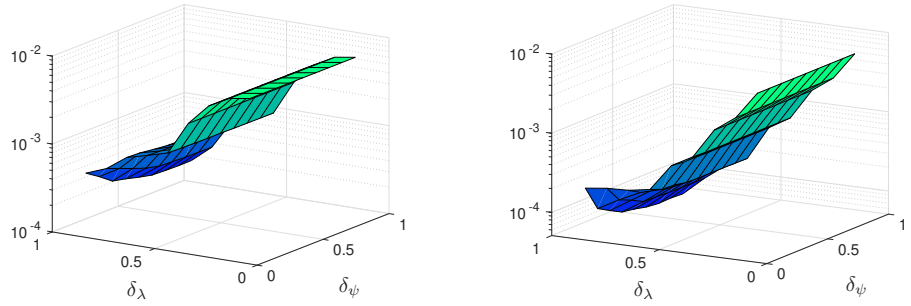

FIG. 10. *DFN*10*: error indicator* Δ_S^h *versus* $\boldsymbol{\delta_\lambda}$ *and* $\boldsymbol{\delta_\psi}$*. Left:* $\boldsymbol{\delta_h} = 0.003$*; right:* $\boldsymbol{\delta_h} = 7.3 \times 10^{-4}$.

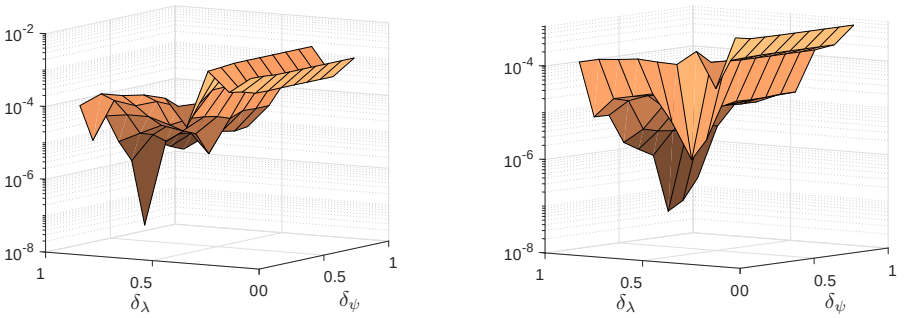

FIG. 11. *DFN*10*: error indicator* $\Delta^{\phi}_{in\text{-}out}$ *versus* $\boldsymbol{\delta_\lambda}$ *and* $\boldsymbol{\delta_\psi}$*. Left:* $\boldsymbol{\delta_h} = 0.003$*; right:* $\boldsymbol{\delta_h} = 7.3 \times 10^{-4}$.

Another error indicator can be introduced, for this configuration, measuring the global flux mismatch between the inflow and the outflow boundary, defined as

$$\Delta^{\phi}_{\text{in-out}} = \frac{|\phi_{\text{in}} - \phi_{\text{out}}|}{\phi_{\text{in}}}, \tag{6.5}$$

where $\phi_{\text{in}}/\phi_{\text{out}}$ is the absolute value of the net flux entering/leaving the network through the inflow/outflow boundary. Given the local flux conservation properties of the method at each trace, this quantity is an error indicator of the global conservation properties. The behavior of $\Delta^{\phi}_{\text{in-out}}$, varying $\boldsymbol{\delta_\lambda}$ and $\boldsymbol{\delta_\psi}$ in the range $[0.1, 0.9]^2$, is shown in Figure 11, for two values of $\boldsymbol{\delta_h}$, with $\boldsymbol{\delta_h} = 0.003$ on the left and $\boldsymbol{\delta_h} = 7.3 \times 10^{-4}$ on the right. It can be seen that the global flux mismatch appears to be affected by variations of $\boldsymbol{\delta_\lambda}$, with a generally decreasing trend for increasing values of this parameter, but also a relevant influence from $\boldsymbol{\delta_\psi}$ appears in this case, mainly at the higher values of $\boldsymbol{\delta_\lambda}$, with a decreasing trend for $\Delta^{\phi}_{\text{in-out}}$ for increasing values of $\boldsymbol{\delta_\psi}$. The quantity $\Delta^{\phi}_{\text{in-out}}$ can be reduced also refining the fracture mesh.

A study on the performances of preconditioners is proposed on this network. Table 2 reports the number of iterations required by the preconditioned conjugate gradient scheme (Algorithm 5.1) to reduce the relative residual up to 10^{-6}, for the nonpreconditioned case and for the preconditioners $\boldsymbol{P_f}$ and $\boldsymbol{P_d}$ described at the end of section 5, for four values of $\boldsymbol{\delta_h}$ and $\boldsymbol{\delta_\lambda} = 0.5$, $\boldsymbol{\delta_\psi} = 0.3$. We can see that using preconditioner $\boldsymbol{P_f}$, the number of iterations needed to reach the required residual is almost unaffected by the value of $\boldsymbol{\delta_h}$ and is only about 3.5% of the number of

TABLE 2
DFN10: number of iterations of PCG algorithm with different preconditioners and mesh refinement; $\boldsymbol{\delta_\lambda} = 0.5$, $\boldsymbol{\delta_\psi} = 0.3$.

N_h	$N_\lambda + N_\psi$	Nonprec.	P_f	P_d
797	69	147	21	49
3120	125	234	22	55
12428	252	457	23	58
49784	502	717	25	62

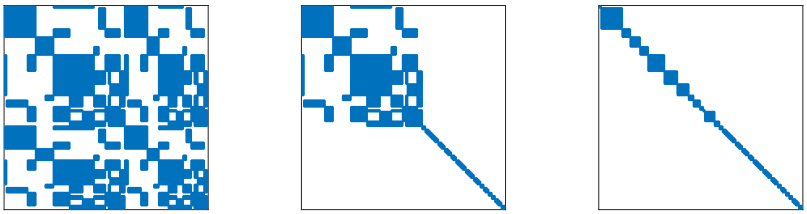

FIG. 12. *DFN10: sparsity pattern of* $\hat{\boldsymbol{G}}$ *and of the preconditioners* $\boldsymbol{P_f}$ *and* $\boldsymbol{P_d}$. *Parameters:* $\boldsymbol{\delta_h} = 0.003$, $\boldsymbol{\delta_\lambda} = 0.5$, $\boldsymbol{\delta_\psi} = 0.3$.

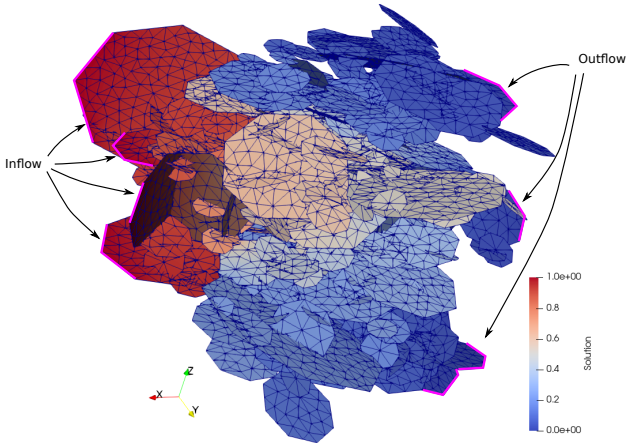

FIG. 13. *DFN395: mesh configuration.*

iterations of the nonpreconditioned case on the finest mesh. The performances of the block-diagonal preconditioner $\boldsymbol{P_d}$, suitable for efficient parallel implementation, are slightly worse than the ones relative to preconditioner $\boldsymbol{P_f}$ but still only marginally affected by mesh refinement and capable of reducing the number of iterations required to convergence to about 8.6% of the number of iterations in the nonpreconditioned case on the finest mesh. The sparsity patterns of the full matrix $\hat{\boldsymbol{G}}$ in (3.29) and of $\boldsymbol{P_f}$ and $\boldsymbol{P_d}$ for mesh parameters $\boldsymbol{\delta_h} = 0.003$, $\boldsymbol{\delta_\lambda} = 0.5$, $\boldsymbol{\delta_\psi} = 0.3$ are shown in Figure 12.

6.3. Realistic DFN problem. As a last example, a DFN consisting of 395 fractures and 629 traces is considered, labeled DFN395. The DFN is obtained as a realization of probability distribution functions on fracture size, orientation, distribution, and hydraulic transmissivity adapted from the data in [35]. The network is shown in Figure 13, along with the inflow and outflow boundary, where Dirichlet

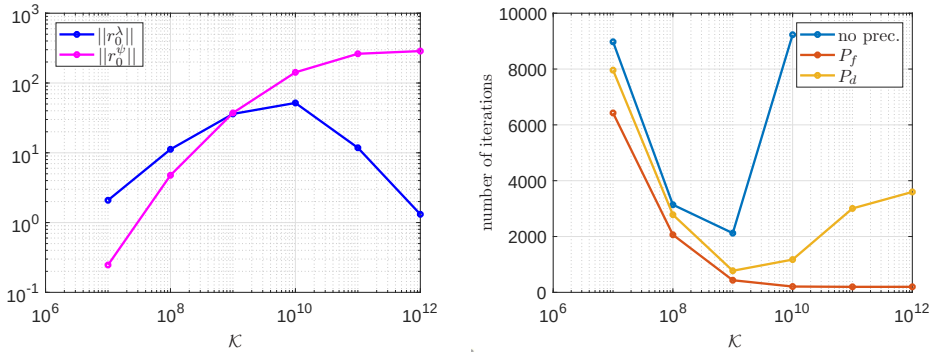

FIG. 14. *DFN395: residual norms* $\|r_0^\lambda\|$ *and* $\|r_0^\psi\|$ *(left) and number of iterations with different preconditioners (right) versus problem scaling.* $\boldsymbol{\delta_h} = 400$ $\boldsymbol{\delta_\lambda} = 0.5$, $\boldsymbol{\delta_\psi} = 0.3$.

boundary conditions of 1 and 0, respectively, are set, all other fracture edges being instead insulated. Two simulations are performed with this geometry and boundary conditions: In a first case a uniform transmissivity equal to $\boldsymbol{K} = 10^{-7}$ is chosen on all fractures, whereas in a second case different, constant transmissivity values are used on each fracture, extracted from a lognormal distribution having mean value of the logarithms equal to $\zeta = -5$ and variance $\frac{1}{3}$.

Let us consider first the case of uniform transmissivity throughout the network: The small value of the transmissivity, compared to the order of magnitude of the hydraulic head, introduces an unbalance among the method's variables, and consequently a rescaling of the problem is beneficial. This is achieved by introducing a scaling factor $\mathcal{K}$ and redefining the constraint equations of the optimization problem replacing transmissivity $\boldsymbol{K}$ by a rescaled transmissivity $\boldsymbol{K}^\star$ given by $K^\star = \mathcal{K}\boldsymbol{K}$, thus obtaining a new problem equivalent to the original one in terms of the hydraulic head but having rescaled fluxes. We refer the reader to [10] for more details on the rescaling, where this methodology has been proposed in a slightly different context.

Let us solve the rescaled problem on a mesh with $\boldsymbol{\delta_h} = 400$, $\boldsymbol{\delta_\lambda} = 0.5$, and $\boldsymbol{\delta_\psi} = 0.3$ for various values of the scaling factor in the range $10^7 < \mathcal{K} < 10^{12}$. Figure 14 shows, on the left, the effect of the scaling on the norm of the initial residual r_0 of the PCG method, split into the part relative to λ, labeled $r_0^\lambda = (r_{0,k})_{k=1,\dots,N_\Lambda}$, and the part relative to ψ, $r_0^\psi = (r_{0,k})_{k=N_\Lambda+1,\dots,N_\Psi}$. Figure 14 displays, on the right, the number of iterations required to solve the problem into a nonpreconditioned relative residual of 10^{-6}, for the nonpreconditioned case and using preconditioners $\boldsymbol{P_f}$ and $\boldsymbol{P_d}$, varying $\mathcal{K}$. In Figure 14, left, we can see that the initial residual norms become similar, i.e., $\|r_0^\lambda\| \approx \|r_0^\psi\|$, for a value of $\mathcal{K} \approx 10^9$. For the same value of $\mathcal{K}$ the number of iterations reaches a minimum, as can be seen in Figure 14, right. At the minimum, the number of iterations required to solve the problem using the preconditioners is reduced by a factor of about 3 with respect to the nonpreconditioned case, and the performances of preconditioners $\boldsymbol{P_f}$ and $\boldsymbol{P_d}$ are quite similar. Using preconditioner $\boldsymbol{P_f}$, the number of iterations for $\mathcal{K} > 10^9$ remains almost fixed, whereas it increases with $\boldsymbol{P_d}$, even if to a small extent if compared to the nonpreconditioned case. Values of $\mathcal{K}$ much larger than the optimal should, however, be avoided, as they are expected to increase the conditioning of the problem.

A rough estimate of the optimal value of $\mathcal{K}$ can be obtained guessing the order of magnitude of the main flux ϕ throughout the network. For the present case, given the chosen boundary conditions, flux essentially occurs along the x-direction, say, $\phi = \phi_x$,

TABLE 3

*DFN*395*, random transmissivity: number of iterations of PCG algorithm and error indicators under mesh refinement and different preconditioning techniques.* $\boldsymbol{\delta_\lambda} = 0.5$ *and* $\boldsymbol{\delta_\psi} = 0.3$.

		No. of iterations			Constraints	
$\boldsymbol{\delta_h}$	$N_\Lambda + N_\psi$	**Nonprec.**	$\boldsymbol{P_f}$	$\boldsymbol{P_d}$	Δ_S^h	$\Delta_{\text{in-out}}^\phi$
1600	2267	2322	443	713	0.0029	0.1128
400	3606	1902	486	757	0.0013	0.0474
100	6946	1727	502	847	0.0006	0.0061

whose order of magnitude can be guessed as $\phi_x = \boldsymbol{K}\frac{\Delta_x h}{L_x}$, with $\Delta_x h$ equal to the hydraulic head difference along the x-direction and L_x the length of the DFN along x, $L_x \approx 1000$, giving $\phi_x \approx 10^{-10}$. As the hydraulic head varies between 1 and 0, it is to be expected that a value of $\mathcal{K}$ around 10^{10} or slightly less should be used to balance the two terms.

Similar results are obtained in the case of different lognormally distributed transmissivities $\boldsymbol{K}_i$ among fractures F_i, $i \in \mathcal{J}$: In this case the order of magnitude of the flux through the network can be guessed as previously, setting $\boldsymbol{K} = 10^\zeta$, where ζ is the mean value of the logarithms of $\boldsymbol{K}_i$, $i \in \mathcal{J}$, obtaining $\phi_x \approx 10^{-8}$. The scaling factor is thus chosen equal to $\mathcal{K} \approx 10^7$ and used for the simulations. Table 3 reports the number of iterations required by the PCG solver to reduce the relative residual norm to 10^{-6} without preconditioning and with the two preconditioners $\boldsymbol{P_f}$ and $\boldsymbol{P_d}$, for different values of $\boldsymbol{\delta_h}$, ranging between 1600 and 100, $\boldsymbol{\delta_\lambda} = 0.5$, $\boldsymbol{\delta_\psi} = 0.3$. The values of the two error indicators measuring continuity of the solution and global flux conservation are also reported in the last two columns. We can see that good performances are achieved by the two preconditioners, which allow one to reduce the number of iterations by a factor up to 5 for preconditioner $\boldsymbol{P_f}$ and up to 3 with preconditioner $\boldsymbol{P_d}$. Both error indicators can be reduced by refining the mesh.

7. Conclusions. A new approach for flow simulations in geometrically complex fracture networks on nonconforming meshes has been formulated and analyzed. The method is based on the minimization of a cost functional expressing the error in continuity of the solution at fracture intersection, constrained by PDEs on the fractures written in a three-field formulation. The resulting discrete problem is well-posed independently of any mesh-related aspect, thus ensuring great flexibility to the method in handling arbitrarily complex networks. A solver based on the preconditioned conjugate gradient is designed for the method, ready for implementation on parallel computing architectures. The effects of mesh parameters on the performances of the method have been thoroughly investigated in the numerical examples, which highlighted, in particular, the key role of parameter $\boldsymbol{\delta_\lambda}$ in controlling the conditioning of the discrete problem. The performances of a preconditioner suitable for parallel implementation have been discussed, also in relation to a reference preconditioner, with a nondiagonal structure. Local and global flux conservation properties and continuity of the solution at fracture intersections have also been analysed. The method has shown to be effective in solving the flow problem in stochastically generated networks.

REFERENCES

[1] P. F. ANTONIETTI, L. FORMAGGIA, A. SCOTTI, M. VERANI, AND N. VERZOTT, *Mimetic finite difference approximation of flows in fractured porous media*, ESAIM: M2AN, 50 (2016), pp. 809–832, https://doi.org/10.1051/m2an/2015087.

[2] M. Benedetto, S. Berrone, A. Borio, S. Pieraccini, and S. Scialò, *A hybrid mortar virtual element method for discrete fracture network simulations*, J. Comput. Phys., 306 (2016), pp. 148–166, https://doi.org/10.1016/j.jcp.2015.11.034.

[3] M. F. Benedetto, A. Borio, and S. Scialò, *Mixed virtual elements for discrete fracture network simulations*, Finite Elem. Anal. Des., 134 (2017), pp. 55–67, https://doi.org/10.1016/j.finel.2017.05.011.

[4] M. Benzi, G. H. Golub, and J. Liesen, *Numerical solution of saddle point problems*, Acta Numer., (2005), pp. 1–137.

[5] B. Berkowitz, *Characterizing flow and transport in fractured geological media: A review*, Adv. Water Resour., 25 (2002), pp. 861–884, https://doi.org/10.1016/S0309-1708(02)00042-8.

[6] S. Berrone, A. Borio, and A. D'Auria, *Refinement strategies for polygonal meshes applied to adaptive VEM discretization*, in Finite Elements in Analysis and Design, 103502, ISSN:0168-874x.

[7] S. Berrone, A. Borio, and F. Vicini, *Reliable a posteriori mesh adaptivity in discrete fracture network flow simulations*, Comp. Methods App. Mech. Engrg., 354 (2019), pp. 904–931, https://doi.org/10.1016/j.cma.2019.06.007.

[8] S. Berrone, S. Pieraccini, and S. Scialò, *A PDE-constrained optimization formulation for discrete fracture network flows*, SIAM J. Sci. Comput., 35 (2013), pp. B487–B510, https://doi.org/10.1137/120865884.

[9] S. Berrone, S. Pieraccini, and S. Scialò, *On simulations of discrete fracture network flows with an optimization-based extended finite element method*, SIAM J. Sci. Comput., 35 (2013), pp. A908–A935, https://doi.org/10.1137/120882883.

[10] S. Berrone, S. Pieraccini, and S. Scialò, *Towards effective flow simulations in realistic discrete fracture networks*, J. Comput. Phys., 310 (2016), pp. 181–201, https://doi.org/10.1016/j.jcp.2016.01.009.

[11] S. Berrone, S. Pieraccini, and S. Scialò, *Non-stationary transport phenomena in networks of fractures: Effective simulations and stochastic analysis*, Comp. Methods Appl. Mech. Engrg., 315 (2017), pp. 1098–1112, https://doi.org/10.1016/j.cma.2016.12.006.

[12] S. Berrone, S. Scialò, and F. Vicini, *Parallel meshing, discretization and computation of flow in massive discrete fracture networks*, SIAM J. Sci. Comput., 41 (2019), pp. C317–C338, https://doi.org/10.1137/18M1228736.

[13] J. Bodin, G. Porel, F. Delay, F. Ubertosi, S. Bernard, and J.-R. de Dreuzy, *Simulation and analysis of solute transport in 2D fracture/pipe networks: The SOLFRAC program*, J. Contam. Hydrol., 89 (2007), pp. 1–28, https://doi.org/10.1016/j.jconhyd.2006.07.005.

[14] F. Brezzi and L. Marini, *A three-field domain decomposition method*, Contemp. Math., 157 (1994).

[15] M. Cacas, E. Ledoux, G. de Marsily, B. Tillie, A. Barbreau, E. Durand, B. Feuga, and P. Peaudecerf, *Modeling fracture flow with a stochastic discrete fracture network: Calibration and validation:* 1. *The flow model*, Water Resour. Res., 26 (1990), pp. 479–489, https://doi.org/10.1029/WR026i003p00479.

[16] F. Chave, D. Di Pietro, and L. Formaggia, *A hybrid high-order method for Darcy flows in fractured porous media*, SIAM J. Sci. Comput., 40 (2018), pp. A1063–A1094, https://doi.org/10.1137/17M1119500.

[17] J. de Dreuzy, G. Pichot, B. Poirriez, and J. Erhel, *Synthetic benchmark for modeling flow in 3D fractured media*, Comput. Geosci., 50 (2013), pp. 59–71.

[18] W. S. Dershowitz and C. Fidelibus, *Derivation of equivalent pipe networks analogues for three-dimensional discrete fracture networks by the boundary element method*, Water Resour. Res., 35 (1999), pp. 2685–2691, https://doi.org/10.1029/1999WR900118.

[19] P. A. Dowd, C. Xu, K. V. Mardia, and R. J. Fowell, *A comparison of methods for the stochastic simulation of rock fractures*, Math. Geol., 39 (2007), pp. 697–714, https://doi.org/10.1007/s11004-007-9116-6.

[20] J. D. Dreuzy, P. Davy, and O. Bour, *Hydraulic properties of two-dimensional random fracture networks following a power law length distribution:* 2. *Permeability of networks based on log-normal distribution of apertures*, Water Resour. Res., 37 (2001), pp. 2079–2095, https://doi.org/10.1029/2001WR900010.

[21] C. Fidelibus, G. Cammarata, and M. Cravero, *Hydraulic characterization of fractured rocks*, in Rock Mechanics: New Research, M. Abbie and J. S. Bedford, eds., Nova Science Publishers, New York, 2009.

[22] A. Fourno, T.-D. Ngo, B. Noetinger, and C. L. Borderie, *Frac: A new conforming mesh method for discrete fracture networks*, J. Comput. Phys., 376 (2019), pp. 713–732, https://doi.org/10.1016/j.jcp.2018.10.005.

[23] A. Fumagalli and E. Keilegavlen, *Dual virtual element method for discrete fractures networks*, SIAM J. Sci. Comput., 40 (2018), pp. B228–B258, https://doi.org/10.1137/16M1098231.

[24] A. Fumagalli, E. Keilegavlen, and S. Scialò, *Conforming, non-conforming and non-matching discretization couplings in discrete fracture network simulations*, J. Comput. Phys., 376 (2019), pp. 694–712, https://doi.org/10.1016/j.jcp.2018.09.048.

[25] A. Hobè, D. Vogler, M. P. Seybold, A. Ebigbo, R. R. Settgast, and M. O. Saar, *Estimating fluid flow rates through fracture networks using combinatorial optimization*, Adv. Water Resour., 122 (2018), pp. 85–97, https://doi.org/10.1016/j.advwatres.2018.10.002, http://www.sciencedirect.com/science/article/pii/S0309170818300666.

[26] J. Hyman, C. Gable, S. Painter, and N. Makedonska, *Conforming Delaunay triangulation of stochastically generated three dimensional discrete fracture networks: A feature rejection algorithm for meshing strategy*, SIAM J. Sci. Comput., 36 (2014), pp. A1871–A1894, https://doi.org/10.1137/130942541.

[27] J. D. Hyman, S. Karra, N. Makedonska, C. W. Gable, S. L. Painter, and H. S. Viswanathan, *DFNworks: A discrete fracture network framework for modeling subsurface flow and transport*, Comput. Geosci., 84 (2015), pp. 10–19, https://doi.org/10.1016/j.cageo.2015.08.001.

[28] S. Karra, D. O'Malley, J. D. Hyman, H. S. Viswanathan, and G. Srinivasan, *Modeling flow and transport in fracture networks using graphs*, Phys. Rev. E, 97 (2018), https://doi.org/10.1103/PhysRevE.97.033304.

[29] B. Nœtinger, *A quasi steady state method for solving transient Darcy flow in complex 3D fractured networks accounting for matrix to fracture flow*, J. Comput. Phys., 283 (2015), pp. 205–223, https://doi.org/10.1016/j.jcp.2014.11.038.

[30] J. Pestana and T. Rees, *Null-space preconditioners for saddle point systems*, SIAM J. Matrix Anal. Appl., 37 (2016), pp. 1103–1128, https://doi.org/10.1137/15M1021349.

[31] G. Pichot, J. Erhel, and J. de Dreuzy, *A generalized mixed hybrid mortar method for solving flow in stochastic discrete fracture networks*, SIAM J. Sci. Comput., 34 (2012), pp. B86–B105, https://doi.org/10.1137/100804383.

[32] G. Pichot, B. Poirriez, J. Erhel, and J. de Dreuzy, *A mortar BDD method for solving flow in stochastic discrete fracture networks*, in Domain Decomposition Methods in Science and Engineering 21, Springer, New York, 2014, pp. 99–112.

[33] M. Sahimi, *Flow and Transport in Porous Media and Fractured Rock*, John Wiley & Sons, New York, 2011, https://doi.org/10.1002/9783527636693.

[34] G. Srinivasan, J. Hyman, D. Osthus, B. Moore, D. O'Malley, S. Karra, E. Rougier, A. Hagberg, A. Hunter, and H. Viswanathan, *Quantifying topological uncertainty in fractured systems using graph theory and machine learning*, Sci. Rep., (2018), https://doi.org/10.1038/s41598-018-30117-1.

[35] A. B. Svensk Kärnbränslehantering, *Data Report for the Safety Assessment SR-Site*, Technical report TR-10-52, Stockholm, Sweden, 2010.

[36] M. Vohralík, J. Maryška, and O. Severýn, *Mixed and nonconforming finite element methods on a system of polygons*, Appl. Numer. Math., 51 (2007), pp. 176–193.